

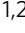


Epigenetic activation of a RAS/MYC axis in H3.3K27M-driven cancer

Sanja Pajovic^{1,6}, Robert Siddaway^{1,6} , Taylor Bridge¹, Javal Sheth¹, Patricia Rakopoulos^{1,2}, Byungjin Kim^{1,2}, Scott Ryall^{1,2}, Sameer Agnihotri³, Lauren Phillips^{1,2}, Man Yu¹, Christopher Li^{1,2}, Scott Milos¹, Palak Patel¹, Dilakshan Srikanthan^{1,2}, Annie Huang^{1,2,4} & Cynthia Hawkins^{1,2,5}  

Histone H3 lysine 27 (H3K27M) mutations represent the canonical oncohistone, occurring frequently in midline gliomas but also identified in haematopoietic malignancies and carcinomas. H3K27M functions, at least in part, through widespread changes in H3K27 trimethylation but its role in tumour initiation remains obscure. To address this, we created a transgenic mouse expressing H3.3K27M in diverse progenitor cell populations. H3.3K27M expression drives tumorigenesis in multiple tissues, which is further enhanced by *Trp53* deletion. We find that H3.3K27M epigenetically activates a transcriptome, enriched for PRC2 and SOX10 targets, that overrides developmental and tissue specificity and is conserved between H3.3K27M-mutant mouse and human tumours. A key feature of the H3K27M transcriptome is activation of a RAS/MYC axis, which we find can be targeted therapeutically in isogenic and primary DIPG cell lines with H3.3K27M mutations, providing an explanation for the common co-occurrence of alterations in these pathways in human H3.3K27M-driven cancer. Taken together, these results show how H3.3K27M-driven transcriptome remodelling promotes tumorigenesis and will be critical for targeting cancers with these mutations.

¹Arthur and Sonia Labatt Brain Tumour Research Centre, The Hospital for Sick Children, Toronto, ON, Canada. ²Department of Laboratory Medicine and Pathobiology, University of Toronto, Toronto, ON, Canada. ³Department of Neurological Surgery, Children's Hospital of Pittsburgh of UPMC, Pittsburgh, PA 15213, United States. ⁴Division of Haematology and Oncology, The Hospital for Sick Children, Toronto, ON, Canada. ⁵Division of Pathology, The Hospital for Sick Children, Toronto, ON, Canada. ⁶These authors contributed equally: Sanja Pajovic, Robert Siddaway. ✉email: cynthia.hawkins@sickkids.ca

Diffuse Intrinsic Pontine Glioma (DIPG) is a devastating paediatric high-grade glioma (HGG) that diffusely penetrates the brainstem and is the leading cause of paediatric brain tumour death¹. Surgery is not possible, radiation is largely palliative, and conventional chemotherapy and targeted agents have proven ineffective. Around 80% of DIPGs harbour lysine 27-methionine (K27M) substitutions in histones H3.3 (*H3F3A*) and H3.1 (*HIST1H3B/C*)^{2,3}. More recently H3K27 mutations have also been found in a range of other tumours including haematopoietic malignancies and carcinomas^{4–8}. Thus, H3K27M is assumed to be an oncohistone, although the precise nature of its oncogenic function remains obscure.

H3K27 is a key hub for transcriptional regulation: acetylation (H3K27ac) is associated with active enhancers while trimethylation (H3K27me3) represses transcription^{9–11}. H3K27M has increased affinity for, and inhibits the activity of, Enhancer of zeste homologue 2 (EZH2), the catalytic subunit of Polycomb repressive complex 2 (PRC2) that deposits H3K27me3, leading to widespread H3K27me3 loss^{12,13}. However, H3K27M also leads to H3K27me3 gains in some areas, suggesting that aberrant gene expression and repression may both be important¹⁴.

Despite clonal analysis indicating that H3K27M is the tumour-initiating mutation in DIPG^{15,16}, *in vivo* models of H3K27M-driven cancer, which to date have focused on brain tumours, have failed to generate tumours without additional oncogenic drivers. The endogenous *H3f3a* locus was modified to allow H3.3K27M expression in Nestin-positive cells, where neonatal H3.3K27M expression decreased the latency of gliomas driven by *Trp53* loss and constitutively active *Pdgfra*¹⁷. In experiments using RCAS-TVA retroviral delivery, neonatal targeting of Nestin-positive brainstem progenitors with H3.3K27M accelerated tumours driven by *Pdgfb* overexpression and *Trp53* loss¹⁸. Similarly, H3.3K27M decreased the latency of glioma formation in *in utero* electroporation experiments introducing H3.3K27M alongside *Trp53* loss, *Pdgfb* overexpression, or WT or constitutively active (D842V) *Pdgfra* overexpression^{19,20}. None of these models yielded tumours where the sole exogenous mutation was H3.3K27M. Further, to produce tumours, H3.3K27M was introduced alongside other strong oncogenic drivers making it difficult to parse out the direct role of the mutant histone in oncogenesis. Overall, these models suggest that H3K27M cooperates with p53 dysfunction and constitutive RAS/MAPK activation, but is not itself sufficient to initiate tumorigenesis, at least in the cells and developmental time points tested thus far. This cooperation with p53 and the RAS/MAPK pathway is supported by the frequent co-occurrence of *PDGFRA* and *TP53* alterations with H3K27M in human DIPGs, although in human tumours H3K27M is clearly the initiating event^{21,22}. Thus, how H3.3K27M alters the cell state to permit or initiate tumorigenesis and the basis of its cooperation with additional mutations remains elusive. A clearer understanding of these mechanisms is critical to developing appropriate therapies for this devastating disease.

Here we used a mouse model expressing H3.3K27M from the *Fabp7* promoter in both neural and non-neural precursor cells to investigate H3K27M-driven cancer. H3.3K27M alone was sufficient to drive development of lymphomas and carcinomas, while *Trp53* loss was required for high grade gliomas to form. H3.3K27M imposed a common transcriptome, mirroring early gliomagenesis, which was shared between H3K27M-driven mouse tumours from all sites, H3.3K27M mouse embryonic brainstem and human DIPGs. A main component of the H3.3K27M transcriptome was an activated RAS/MYC axis which could be targeted therapeutically. H3K27M-mutant tumours acquired secondary mutations to reinforce this activation, suggesting a model where early epigenetic pathway activation by H3K27M is later reinforced by pathway activating genetic

mutations and explaining the co-occurrence of these mutations in human DIPG.

Results

H3.3K27M increases cancer incidence and leads to early death.

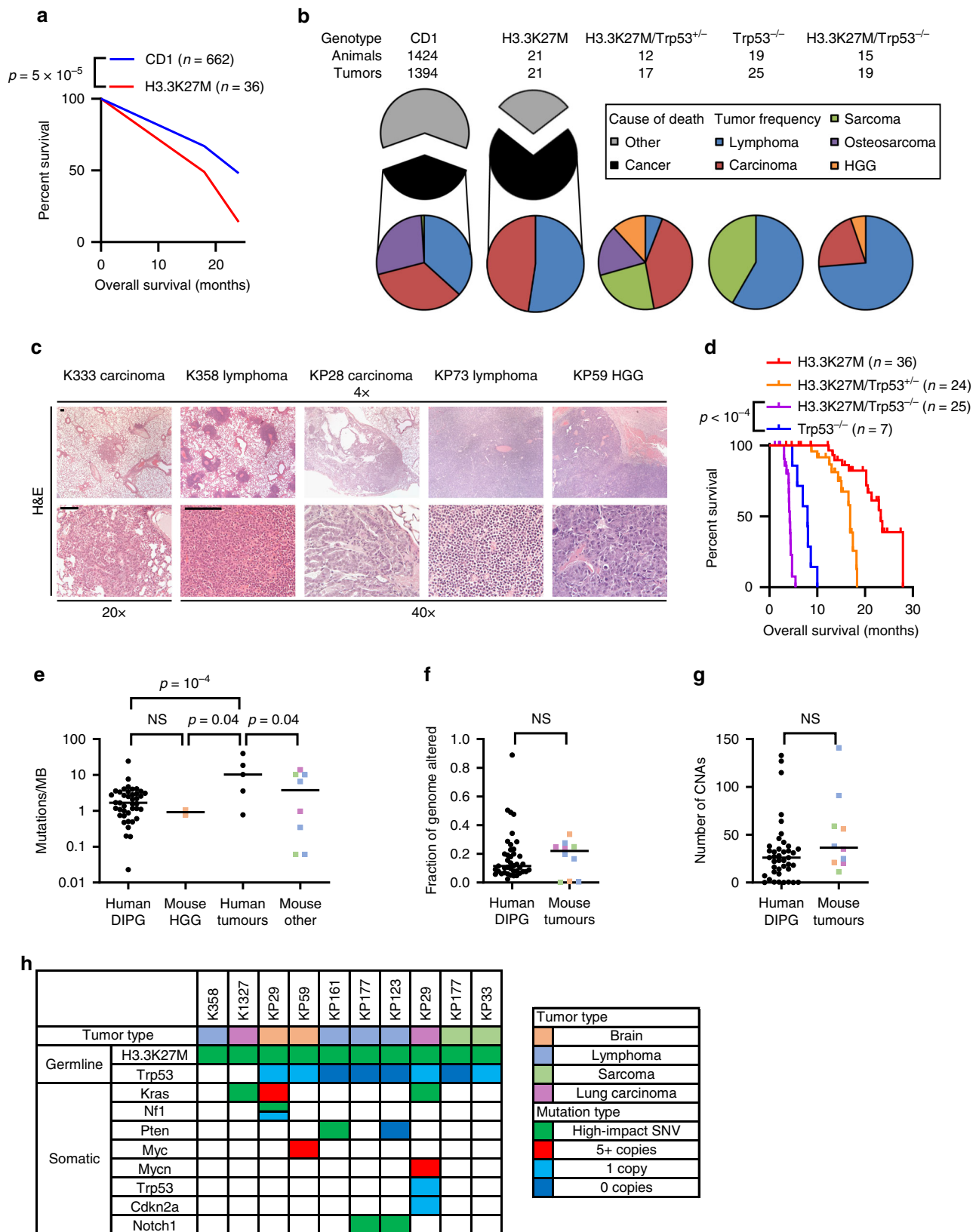
CD-1 mice, expressing FLAG/HA-tagged H3.3K27M (*H3f3a-K27M*) under the control of the *Fabp7* promoter, were engineered by microinjection, with colonies established from 3 founders (Supplementary Fig. S1a–c). *Fabp7* promoter-directed H3.3K27M expression was compatible with viable embryonic and postnatal development; adult mice had similar phenotype and litter size to CD1 wild-type mice, although E12.5 and E14.5 H3.3K27M-positive embryos occasionally developed signs of central nervous system haemorrhage (Supplementary Fig. S1d). At the gene expression level, *Fabp7* expression is highest in brain during embryogenesis, but is expressed in adult brain as well as in other embryonic and adult tissues including liver, intestine, heart, lung and bone (Supplementary Fig. S1e). Correspondingly, we saw that H3.3K27M expression was highest in brain, yet readily detectable in other tissues (Supplementary Fig. S1f, g)^{23–26}. Importantly, the H3.3K27M-FLAG/HA transgene was not overexpressed versus endogenous H3.3 in the mouse samples or when compared to H3K27M levels in human DIPG (Supplementary Fig. S1h, i).

H3.3K27M mice had 62% reduced survival (all-cause mortality) compared to CD1 controls at two years ($p = 5.5 \times 10^{-5}$; Fig. 1a, Supplementary Data 2)²⁷, and were 67% more likely to die from cancer ($p = 0.005$; Fig. 1b). They had a 2.7-fold increase in both lymphoma ($p = 3.1 \times 10^{-4}$) and carcinoma ($p = 9.6 \times 10^{-4}$) compared with controls (Fig. 1b, Supplementary Data 2)^{28–30}. H3.3K27M lymphomas most frequently involved the mediastinum (45%) and were disseminated in 36% of mice, with immunophenotyping showing them to be T-cell lymphomas (B220⁻/CD3⁺; Supplementary Fig. S2a). Carcinomas were usually adenocarcinoma and primarily involved the lung (Fig. 1c), with significantly increased incidence in H3.3K27M mice compared with CD1 controls ($p = 0.02$). Both lymphomas and carcinomas expressed H3.3K27M and FABP7, indicating that they were driven by transgene expression rather than forming spontaneously (Supplementary Fig. S2b). Together, this indicates that H3.3K27M expression drives a significantly increased incidence of lymphoma ($p = 4.2 \times 10^{-4}$) and carcinoma ($p = 0.001$) in mice. This is the first evidence that H3.3K27M alone can cause cancer and that it functions as a pan-cancer driver.

H3.3K27M induces gliomas and increases lymphomagenesis in *Trp53*-deficient mice.

As H3.3K27M and *TP53* alterations are highly co-associated in human gliomas, we crossed H3.3K27M mice with *Trp53*^{+/-} deficient animals. Morphologic and immunophenotypic high grade gliomas (HGG) developed at low penetrance in both H3.3K27M/*Trp53*^{+/-} and H3.3K27M/*Trp53*^{-/-} mice, but not in H3.3K27M, *Trp53*^{+/-} or *Trp53*^{-/-} mice (Fig. 1b, c and Supplementary Fig. S2c, Supplementary Data 2). Most had leptomeningeal dissemination, with tumour masses involving the cerebellum, cerebral hemispheres and/or base of the third ventricle. A similar proportion (~70%) of mouse HGG and human DIPG overexpressed *OLIG2* (Supplementary Fig. S2c, d).

H3.3K27M/*Trp53*^{-/-} mice developed more lymphomas (56%) than H3.3K27M (42%) or *Trp53*^{-/-} (32%) animals, and had a 2-fold reduced median survival compared with *Trp53*^{-/-} mice ($p < 0.0001$; Fig. 1b, d, Supplementary Data 2)^{31,32}. All tumours in H3.3K27M mice, regardless of tissue of origin, maintained H3.3K27M expression (Supplementary Fig. S2b). Overall, H3.3K27M mice have increased cancer incidence with decreased latency, with gliomas and lymphomas both increased by *Trp53* loss.



H3.3K27M-driven mouse and human tumours have similar genomic features. We performed whole exome sequencing (WES) on 10 tumours from 8 H3.3K27M, H3.3K27M/Trp53^{+/-} or H3.3K27M/Trp53^{-/-} mice to investigate the evolution of H3.3K27M-driven tumorigenesis. We compared the genetic features of the H3.3K27M mutant mouse tumours with those of

human brain and non-brain tumours. The mutation frequency was similar between mouse and human tumours (Fig. 1e, Supplementary Data 3)^{5,21}. The burden of copy number variations (CNV) and the fraction of the genome affected by CNVs was also similar between mouse tumours and human H3.3K27M DIPG (Fig. 1f, g and Supplementary Fig. S2e; Supplementary Data 3)²¹.

Fig. 1 H3.3K27M drives tumorigenesis with genomic changes consistent with DIPG. **a** Survival plot (all-cause mortality) of H3.3K27M mice (red line, $n = 36$) versus CD1 control mice (blue line, $n = 662$)²⁷. Significance was determined at 24 months. **b** Pie charts showing the percentage deaths of H3.3K27M and CD1 mice (top, CD1 data from^{28–30}) arising from cancer (black) or other causes (grey). The frequency of different tumour types amongst the cancer-related deaths are shown in the coloured pie charts for each genotype where red=carcinoma, blue=lymphoma, purple=osteosarcoma, green=other sarcoma and orange=high grade glioma (HGG) (bottom). **c** Haematoxylin and Eosin (H&E) staining of representative tumours from H3.3K27M mice. Scale bar: 100 μm . **d** Kaplan-Meier survival analysis of H3.3K27M, H3.3K27M/*Trp53*^{+/-}, H3.3K27M/*Trp53*^{-/-} and *Trp53*^{-/-} mice³¹. **e** Somatic mutation burden (single-nucleotide variants/indels per megabase (MB) of exome) of human DIPG ($n = 41$), mouse HGG ($n = 2$), and human ($n = 5$) and mouse ($n = 8$) non-gliomas. Mouse tumours are coloured by type as in **h**. **f** Comparison of the fraction of the genome altered between human DIPG ($n = 41$) and mouse ($n = 10$) tumours. Mouse tumours are coloured by type as in **h**. **g** Comparison of copy number alteration (CNA) burden between human DIPG ($n = 41$) and mouse ($n = 10$). Mouse tumours are coloured by type as in **h**. **h** Oncoprint of tumour type, H3.3K27M and *Trp53* genotype plus specific SNVs and focal CNAs. Source data are provided as a Source Data file. Statistical tests: Yates' Chi-squared (**a**), log rank (**d**), t (**e**, **f**, **g**). NS: Not significant.

Further analysis showed that SNVs and CNVs were acquired in known driver genes of human cancer (including DIPG). These included *Kras* (HGG, carcinoma), *Nf1* (HGG), *Pten* (carcinoma), *Myc* (HGG, carcinoma) and *Notch* (lymphoma) (Fig. 1h). Interestingly, somatic *Trp53* alterations were acquired in 2 tumours, highlighting the cooperative importance of p53 dysfunction in H3.3K27M-driven tumorigenesis. KP29 (H3.3K27M^{+/-}) lung carcinoma lost the copy of chromosome 11 (Supplementary Fig. S2e) carrying the wild-type *Trp53* allele, resulting in a *Trp53*^{-/-} tumour, while K1327 (*Trp53*^{+/+}) lung carcinoma acquired an R62Q mutation in the p53 transactivation domain, which is critical for apoptotic signalling (Supplementary Fig. S2f)³³. The latter was detected by Sanger sequencing but with a low mutant allele frequency by WES, indicating that it was a sub-clonal, presumably later-occurring, variant. Overall, H3.3K27M mouse tumours show similar mutation patterns to human DIPG, with frequent mutations in the RAS/MAPK/PI3K pathway (50%) and MYC (20%; Fig. 1h).

H3.3K27M rapidly disrupts transcriptional networks to establish a glioma-like, proliferative phenotype in mid-development in cooperation with SOX10. In order to investigate the earliest events resulting from H3.3K27M expression we examined brainstem tissue from E14.5 mouse embryos, ~5 days after H3.3K27M expression is induced from the *Fabp7* promoter. We further generated isogenic cell lines expressing H3.3K27M or empty vector (EV) using the human oligodendrocyte precursor cell (OPC) line MO3.13, as OPCs are a proposed cell of origin for DIPG³⁴.

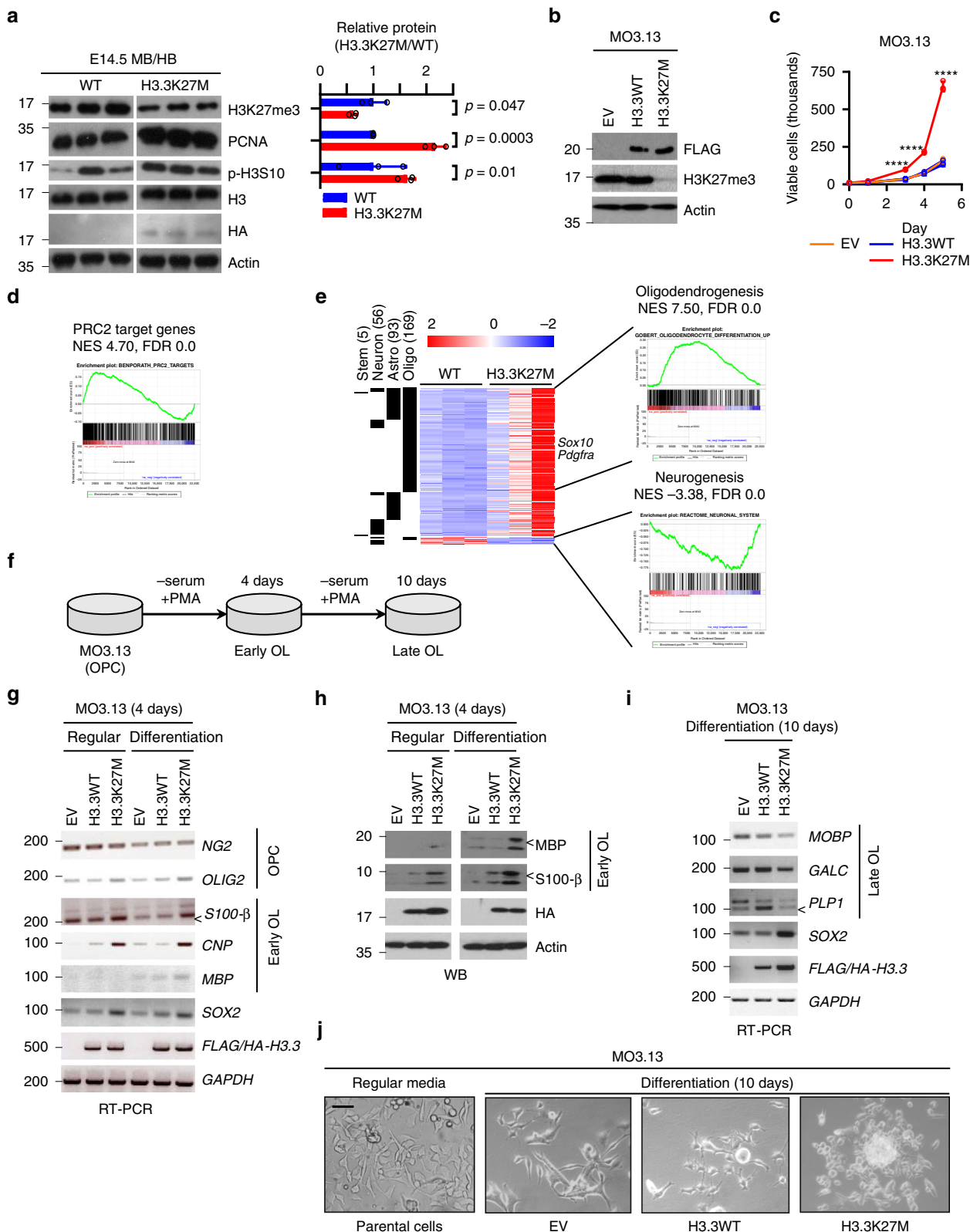
H3.3K27M has an inhibitory effect on PRC2, and its expression in E14.5 midbrain/hindbrain (MB/HB) or MO3.13 cells reduced H3K27me3 compared to controls (Fig. 2a, b and Supplementary Fig. S3a). This was accompanied by an increase in the proliferative markers PCNA and phospho-H3S10 in H3.3K27M mice compared with WT (Fig. 2a). A similar increase in proliferation was seen in the MO3.13 cells compared with empty vector (EV) and H3.3WT-expressing control cells (Fig. 2c). In a scratch assay, while EV and H3.3WT cells failed to close a wound after 24 h, H3.3K27M-expressing MO3.13 cells had fully closed the wound, further suggesting that H3.3K27M confers pro-tumorigenic behaviour on MO3.13 cells (Supplementary Fig. S3b).

To better understand the acute transcriptional effects of H3.3K27M expression and the proliferative E14.5 phenotype, we performed RNA sequencing (RNA-Seq), identifying 992 up- and 50 down-regulated genes differentially expressed between H3.3K27M and WT MB/HB at E14.5 (Supplementary Fig. S3c, Supplementary Data 1). H3.3K27M expression level strongly correlated with the degree of gene upregulation (Pearson's correlation 0.999, $p = 0.001$; Supplementary Fig. S3d, e). In keeping with the known inhibitory effect of H3.3K27M on PRC2,

gene set enrichment analysis (GSEA) revealed significantly increased expression of known PRC2 target genes (Fig. 2d), including the PRC2-repressed *Hox* gene family that has important functions in brain development (Supplementary Fig. S3f, g)^{35,36}. By chromatin-immunoprecipitation (ChIP) we found that the *Hoxa3*, *Hoxb4* and *Hoxc8* promoters had reduced H3K27me3 in H3.3K27M MB/HB compared with WT (Supplementary Fig. S3h) suggesting that H3.3K27M upregulates them via PRC2 inhibition. H3.3K27M expression in MO3.13 cells also resulted in *Hoxb4* upregulation (Supplementary Fig. S3i).

Fewer than 10% of the significantly upregulated genes were direct PRC2 targets as defined in MSigDB^{37,38} indicating that, despite the importance of PRC2 in H3K27M function, pathways beyond PRC2 are also relevant to the transforming effects of H3K27M (Figs. 3a, 5a and Supplementary Fig. S4a). Among the upregulated expressed genes at E14.5, nearly 20% were associated with OPCs/oligodendrocyte differentiation, <10% with astrocyte differentiation and very few with neuronal differentiation or NSCs (Fig. 2e and Supplementary Fig. S4b)³⁹. Promoters of neuronal differentiation were downregulated, while several inhibitors of neurogenesis were upregulated (Fig. 2e and Supplementary Fig. S4c)³⁹. Oligodendrogenic markers (OLIG1, OLIG2, O4) were increased at both E14.5 and E16.5, neuronal markers (TUF1, DCBN) were decreased at E14.5 and the astrocyte marker GFAP was unchanged (Supplementary Fig. S4d), suggesting that H3.3K27M affects cell specification.

To evaluate the potential of H3.3K27M to regulate oligodendrocyte transcriptional programmes, we differentiated MO3.13 OPCs into oligodendrocytes (OL) using serum starvation and phorbol 12-myristate 13-acetate (PMA)⁴⁰, as monitored by decreasing NG2 expression (Fig. 2f, g). S100 calcium binding protein beta (S100- β), myelin basic protein (MBP) and 2',3'-cyclic nucleotide 3'-phosphodiesterase (CNP), which are upregulated during OPC differentiation into immature/early OL^{41–43}, were induced by H3.3K27M expression and maintained after treatment with differentiation media for 4 days (Fig. 2g, h). SOX2, a marker of undifferentiated and cancer stem cells that is increasingly implicated in numerous oncogenic processes⁴⁴, was also induced in H3.3K27M, but not in EV or H3.3WT cells, in both regular and differentiation media (Fig. 2g). This suggested that H3.3K27M may subvert the differentiation process and prompted us to extend differentiation treatment to 10 days (Fig. 2f). The late OL markers myelin associated oligodendrocyte basic protein (MOBP), galactosylceramidase (GALC) and proteolipid protein 1 (PLP1) were expressed in EV and H3.3WT cells with changes in morphology consistent with OL differentiation as compared with MO3.13 cells grown in regular media (Fig. 2i, j). In contrast, H3.3K27M cells were SOX2-high, late-OL marker-low, and had a morphology consistent with undifferentiated cells including neurosphere formation (Fig. 2i, j). Taken together, this data implies that H3.3K27M subverts the OPC transcriptome and



differentiation programme to promote early/mid OL gene expression but not terminal differentiation, instead continuing to drive proliferation and induce characteristics of undifferentiated cells.

While loss of H3K27me3 is permissive for gene transcription, this loss alone is not enough; transcriptional upregulation is also dependent on the presence of transcription factors. We combined

differential gene expression, transcription factor binding sites and protein-protein interactions to identify potential master regulators of the H3K27M phenotype. We found that the transcription factor SOX10 directly regulates ~30% of genes upregulated by H3.3K27M in E14.5 MB/HB, 3.4x more than are direct PRC2-targets (Fig. 3a). SOX10 influences lineage commitment in the developing brain to promote oligodendrogenesis⁴⁵, and we noted

Fig. 2 H3.3K27M rapidly induces a glioma-like proliferative phenotype in developing brainstem and subverts oligodendrocyte differentiation programmes. **a** Western blot of H3.3K27M and WT MB/HB from littermates harvested at E14.5. Densitometry quantifies H3.3K27M versus WT (normalised to actin) and is plotted as mean \pm standard deviation ($n = 3$ independent embryos). **b** Western blot of empty vector (EV), H3.3WT or H3.3K27M MO3.13 cells (results are representative of 2 independent experiments from different litters). **c** Growth curve of MO3.13 cells transduced with empty vector (EV) or H3.3K27M. Bars show mean \pm standard deviation ($n = 3$). **d** GSEA (gene set enrichment analysis) of BENPORATH_PRC2_TARGETS gene set in H3.3K27M E14.5 MB/HB. NES: Normalised Enrichment Score. FDR: false discovery rate. **e** Heatmap and GSEA of differentially expressed genes in H3.3K27M E14.5 MB/HB with functions in different lineages. Oligo: oligodendrocyte, Astro: astrocyte. **f** Schematic of experiment differentiating MO3.13 cells from oligodendrocyte precursor cells (OPC) into early and late oligodendrocytes (OL) experiment using serum starvation and (PMA) phorbol 12-myristate 13-acetate treatment. **g** RT-PCR analysis of MO3.13 cells grown in regular media or differentiated for 4 days. <: specific band. Results are representative of 6 independent replicates. **h** Western blot of MO3.13 cells grown in regular media or differentiated for 4 days. <: specific band. Results are representative of 2 independent replicates. **i** RT-PCR analysis of MO3.13 cells grown in regular media or differentiated for 10 days. <: specific band. Results are representative of 2 independent replicates. **j** Bright-field microscopy images of MO3.13 cells grown in regular media or differentiated for 10 days. Results are representative of 2 independent replicates. Scale bar: 100 μ m. Source data are provided as a Source Data file. Statistical tests: t (**a**, **c**). *** $p < 0.0001$.

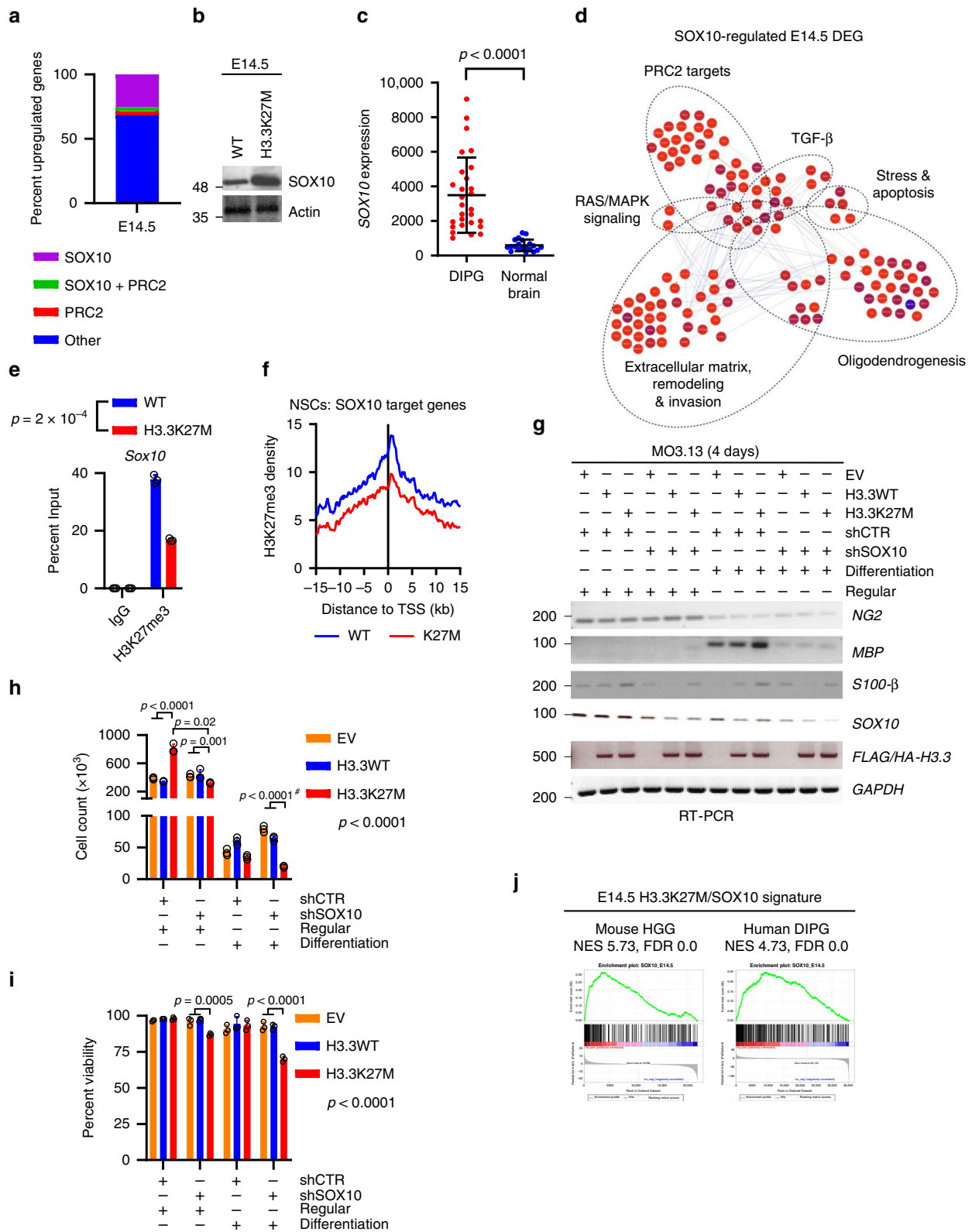
that it was upregulated in H3.3K27M MB/HB at E14.5 (Figs. 2e, 3b and Supplementary Fig. S4b, e) as well as H3.3K27M-expressing MO3.13 cells and human H3.3K27M-mutant DIPG (Fig. 3c and Supplementary Fig. S3i), suggesting it may cooperate with H3.3K27M. The genes regulated by SOX10 play key roles in many important biological processes that may be important for mediating the oncogenic function of H3.3K27M (Fig. 3d). A reduction in H3K27me3 at the *Sox10* promoter in H3.3K27M E14.5 MB/HB and throughout the promoter and gene body of H3.3K27M-expressing NSCs⁴⁶ (Fig. 3e and Supplementary Fig. S4f) suggested that H3.3K27M epigenetically mediates SOX10 upregulation through H3K27me3 loss. Furthermore, H3.3K27M-expressing NSCs exhibited significant loss of H3K27me3 in the promoters of *Sox10* target genes (Fig. 3f)⁴⁶. Overall, the majority of genes upregulated in the early response to H3.3K27M are not canonical PRC2 target genes. This data suggests that SOX10 may be at least partially responsible for mediating this early response in the MB/HB by promoting oligodendrogenic expansion at the expense of neuronal differentiation.

To better understand how H3.3K27M and SOX10 interact we depleted SOX10 expression in MO3.13 cells (Supplementary Fig. S4g), and repeated the 4-day differentiation assay (Fig. 2f). *S100- β* and *MBP* are both SOX10 target genes⁴². H3.3K27M did not induce expression of these genes after SOX10 knockdown, confirming the importance of SOX10 in executing the H3.3K27M transcriptome (Fig. 3g). As expected, all differentiation conditions decreased cell proliferation ($p < 0.0001$; Fig. 3h and Supplementary Fig. S4h). Strikingly, SOX10 depletion reversed the growth advantage conferred by H3.3K27M in regular media and, when combined with differentiation media, H3.3K27M cells grew substantially more slowly than EV and H3.3WT controls ($p < 0.0001$ when normalising by EV condition to control for the dominating media effect; Fig. 3h and Supplementary Fig. S4h). Moreover, SOX10 depletion had a synthetic lethal effect with H3.3K27M expression, particularly under differentiation conditions, while EV and H3.3WT cell viability was unaffected ($p < 0.0001$; Fig. 3i and Supplementary Fig. 4i). Collectively these data suggest that H3K27M co-operates with SOX10 in the regulation of transcription programmes involved in cell fate, proliferation, and survival of OL cells consistent with our findings in H3K27M brains, mouse HGGs, and human DIPGs. In keeping with this, the H3.3K27M/SOX10 signature was highly upregulated in both H3.3K27M-mutant mouse HGG and human DIPG (Fig. 3j). Furthermore, 20–30% of differentially expressed genes in the E14.5, mouse HGG and human DIPG datasets are SOX10 target genes, suggesting that SOX10 activity is maintained throughout tumorigenesis.

To further investigate the similarities between the early effects of H3.3K27M on the brainstem and gliomagenesis we compared the transcriptomes of H3.3K27M mutant E14.5 brainstem with H3.3K27M/Trp53^{+/-} mouse HGGs and human DIPGs. The differentially expressed genes and pathways in all 3 datasets were strikingly similar (all two-way overlaps $p \leq 10^{-7}$; Fig. 4a, b). 167 commonly regulated genes were enriched in extracellular remodelling pathways, consistent with the highly invasive nature of human DIPG (Fig. 4c), and 52 were SOX10 target genes, underscoring the importance of SOX10 activity in establishing the early transcriptional response to H3.3K27M that is maintained throughout tumorigenesis ($p = 10^{-56}$, Fig. 4d). The 53 pathways commonly regulated across all 3 datasets included proliferative (RAS signalling, cell cycle, MYC), extracellular remodelling (epithelial-mesenchymal transition, adhesion) and metabolic (glycolysis, oxidative phosphorylation) terms. All 3 datasets showed strong enrichment of the mesenchymal subtype and strong repression of neural/proneural glioblastoma subtype signatures (Fig. 4e)⁴⁷. These data suggest that H3.3K27M rapidly establishes a transcriptome in the brainstem that recapitulates features of gliomagenesis.

H3.3K27M drives a core transcriptome in different cellular contexts.

To understand the effect of H3.3K27M in different tissues we compared RNA-Seq of HGG, lymphoma and brain from H3.3K27M mice with adult wild-type mouse brain, spleen, thymus and bone marrow⁴⁸, as well as human DIPG and normal brain. Single-sample GSEA (ssGSEA) was used to analyse relative pathway activity across different samples. T-stochastic neighbour embedding (t-SNE) models and hierarchical clustering revealed that, while brain samples clustered separately from bone marrow, spleen and thymus, reflecting expected inter-tissue transcriptional differences, H3.3K27M-driven tumours clustered together, distinctly from their tissues of origin (Fig. 4f and Supplementary Fig. S5a). Similarly, mouse H3.3K27M HGG and lymphomas grouped with human H3.3K27M DIPG, while control H3.3K27M adult mouse brain samples grouped with normal human brain (Fig. 4g). This suggests that H3.3K27M establishes a transcriptome that is conserved across tumour types and overrides tissue-specific expression patterns. Gene sets or transcriptional pathways commonly regulated between H3.3K27M mouse HGG, H3.3K27M mouse lymphoma and human DIPG included RAS, PI3K/AKT signalling and MYC targets (Figs. 4h, 4i, 5a and Supplementary Fig. S5b). Finally, we asked whether the H3.3K27M-SOX10 axis (Fig. 3) has a role in regulation of these pathways. Except for MYC targets at E14.5, which were not upregulated at E14.5 and therefore have no overlap with SOX10-regulated genes at this



developmental stage, 30–40% of the RAS/MYC targets and ECM genes differentially expressed in each of H3.3K27M E14.5 MB/HB, mouse HGG and human DIPG are SOX10 target genes (Supplementary Fig. S5c).

Recent data has suggested repression of *CDKN2A* may be important in H3.3K27M-mediated tumorigenesis, as this gene retains its promoter H3K27me3 in the presence of the

oncohistone, and the expression level of p16 regulates the proliferative capacity of H3.3K27M-mutant cells^{18,46}. We examined *Cdkn2a* promoter H3K27me3 in E14.5 MB/HB, finding that H3.3K27M reduced *Cdkn2a* methylation at this developmental time point (Supplementary Fig. S5d). There was not an accompanying expression change in *Cdkn2a* in RNA-Seq data and, in our mouse HGG and human DIPG datasets, it was

Fig. 3 SOX10 is important for the early response to H3.3K27M and activates a signature maintained in gliomas. **a** Percentage of upregulated genes in H3.3K27M E14.5 MB/HB that are directly regulated by PRC2 and/or SOX10. **b** Western blot of H3.3K27M and WT MB/HB from littermates harvested at E14.5. Note that the actin loading control is shared with Fig. 5e (results are representative of at least 3 independent experiments). **c** SOX10 expression in human H3.3K27M DIPG ($n = 28$) and normal brain ($n = 20$). **d** Network diagram showing SOX10 transcriptional targets from key pathways that are differentially expressed at E14.5. Red: upregulated genes; blue: downregulated genes; colour intensity reflects expression fold-change. DEG: differentially expressed gene. **e** ChIP quantifying H3K27me3 at the *Sox10* promoter in E14.5 WT or H3.3K27M MB/HB. **f** H3K27me3 ChIP-Seq density was profiled ± 15 kb around the (transcription start site) TSS of SOX10 target genes in H3.3K27M or H3.3WT NSCs⁴⁶. **g** RT-PCR analysis of MO3.13 cells transduced with control (shCTR) or SOX10-specific (shSOX10) shRNA and grown for 4 days in regular or differentiation media. Results are representative of 6 independent replicates (shSOX10 clone 1 $n = 2$, clone 2 $n = 4$). EV: empty vector. **h** Cell counts of MO3.13 cells grown as in **g**. Bars show mean \pm standard deviation ($n = 3$). **i** Percent viability of MO3.13 cells grown as in **g**. Bars show mean \pm standard deviation ($n = 3$). #significance for EV vs H3.3K27M in shSOX10 cells grown in differentiation media was tested by normalising each condition by EV to control for media effect. **j** SOX10 target genes upregulated in H3.3K27M E14.5 MB/HB were used for gene set enrichment analysis (GSEA) in H3.3K27M mouse HGG and human DIPG. Source data are provided as a Source Data file. Statistical tests: t (**c**, **e**), ANOVA (**h**, **i**).

upregulated (Supplementary Fig. S5e, f), suggesting that p16 repression is not a key feature of tumorigenesis in this mouse model.

RAS/MAPK activation is an early response to H3.3K27M. RAS signalling was one of the most strongly activated pathways in established H3.3K27M mouse HGG and lymphoma as well as human DIPG (Fig. 4h, i and Supplementary Fig. S5b). To ask if this was an early response to H3.3K27M, we examined E14.5 MB/HB. At this time point H3.3K27M had been expressed for ~ 5 days and a proliferative phenotype established (Fig. 2a). Western blotting and RNA-Seq analysis of E14.5 mouse brainstem revealed that RAS/MAPK signalling was indeed already activated in an H3.3K27M associated manner (Fig. 5a–c). *Pdgfra*, one of the main receptors activating RAS signalling, was upregulated in H3.3K27M E14.5 MB/HB, as well as in mouse HGG and human DIPG (Fig. 5d–f and Supplementary Fig. S5h), and the promoters of *Pdgfra*, *Hras*, *Kras* and *Nras* had reduced H3K27me3 at E14.5 (Fig. 5g and Supplementary Fig. S5i). MO3.13 cells expressing H3.3K27M had increased MEK and ERK phosphorylation compared with their empty vector (EV) counterparts (Fig. 5h). H3.3K27M markedly reduced H3K27me3 in the promoters of RAS target genes in NSCs (Fig. 5i)⁴⁶.

This data suggested that H3.3K27M drives epigenetic activation of the RAS/MAPK pathway by targeting multiple pathway members and its downstream target genes. To further test the dependence of the RAS/MAPK pathway activation on H3.3K27M expression, we next examined H3.3K27M-mutant primary paediatric HGG (pHGG) BT245 cells in which the H3.3K27M mutation had been reversed using CRISPR⁴⁹. BT245-M27K cells showed increased H3K27me3 in the promoters of RAS target genes and significantly downregulated their expression compared with parental H3.3K27M-mutant BT245 cells (Fig. 6a, b). Similarly, depletion of *H3F3A* by shRNA in (*H3F3A*-K27M) H3.3K27M-mutant primary DIPG cells restored RAS target gene promoter H3K27me3 (Supplementary Fig. S6a)⁵⁰. In H3-WT G477 pHGG cells overexpressing H3.3K27M or H3.3K27R⁴⁹, K27R had no effect on H3K27me3 while K27M upregulated RAS target genes and decreased their promoter H3K27me3 (Fig. 6c and Supplementary Fig. S6b). Finally, in a panel of primary pHGG cells, H3.3K27M-mutant cells had reduced RAS target gene promoter H3K27me3 compared with H3WT cells (Fig. 6d)⁴⁹. Together, this suggests that H3.3K27M-mutant tumours exhibit K27M-mediated epigenetic activation of the RAS/MAPK pathway.

Early epigenetic activation of RAS/MAPK pathway is later reinforced by genetic activation. Based on sequencing data it is well established that mutations in the RAS/MAPK pathway are

frequent events in human DIPG⁵¹ suggesting activation of this pathway is an important step in DIPG tumorigenesis with clonal evolution modelling implicating these as later events^{15,16}. Interestingly, our RNAseq data showed activation of the RAS/MAPK pathway in both mouse tumours and human DIPG regardless of whether the RAS/MAPK/PI3K pathway was mutated (Fig. 6e–g, Supplementary Fig. S6c and S6d) suggesting that activation of this pathway may be universal with epigenetic/non-mutation-dependent mechanisms responsible for this activation in the non-mutant cases. Intriguingly, in another mouse model where H3.3K27M accelerated development of *Trp53*^{KO}/*Pdgfra*-driven HGG¹⁷, the addition of H3.3K27M epigenetically activated RAS target genes compared to the H3.3WT HGG despite the pathway already being activated by constitutively active PDGFRA (Supplementary Fig. S6e, f)¹⁷ suggesting epigenetic mechanisms of pathway activation may play a role, even in mutant tumours.

The rapid induction of a RAS/MAPK signalling signature in both our mouse and cell line models following introduction of H3.3K27M as detailed above suggests that epigenetic activation of the pathway may be an early event, with mutation-dependent activation occurring later in tumour development or in a subclonal fashion. This is consistent with a model where the early epigenetic activation of RAS by H3.3K27M is later reinforced by genetic activation of the pathway.

To test if RAS/MAPK genetic alterations in the H3.3K27M mouse tumours are early or late events we investigated the clonal evolution of these tumours (Fig. 6h). For the KP29 HGG and lung carcinoma this also provided a unique opportunity to understand how H3.3K27M affects tumorigenesis of two different tissues within the same animal. These two tumours had little genetic similarity, indicating that both were primary (Fig. 1h and Supplementary Fig. S2e). RAS was activated in both tumours, with *Kras* alterations in the second and first clone of the HGG and lung carcinoma, respectively (Fig. 6h). The HGG additionally had a single copy *Nf1* deletion in clone 1. The lung carcinoma also acquired a focal *Mycn* amplification and single-copy chromosome 11 (*Trp53*) loss in the first clone, and a broad single-copy loss in chromosome 4, containing *Cdkn2a*, in the second (Fig. 6h). Overall, as with human DIPG, most H3.3K27M-driven mouse tumours acquire additional, subclonal, oncogenic alterations beyond the truncal histone mutation and *Trp53* loss. Intriguingly, these alterations converge on the RAS/MAPK/PI3K pathway and MYC/MYCN, which are key features of H3.3K27M DIPG²¹.

Epigenetic activation of a RAS/MYC axis in H3.3K27M-driven cancer. MYC target genes were among the most upregulated gene sets in H3.3K27M mouse HGG and lymphomas, and human DIPGs (Fig. 4h, i and Supplementary Fig. S5b). As with RAS signalling, H3.3K27M mouse HGG and human DIPG

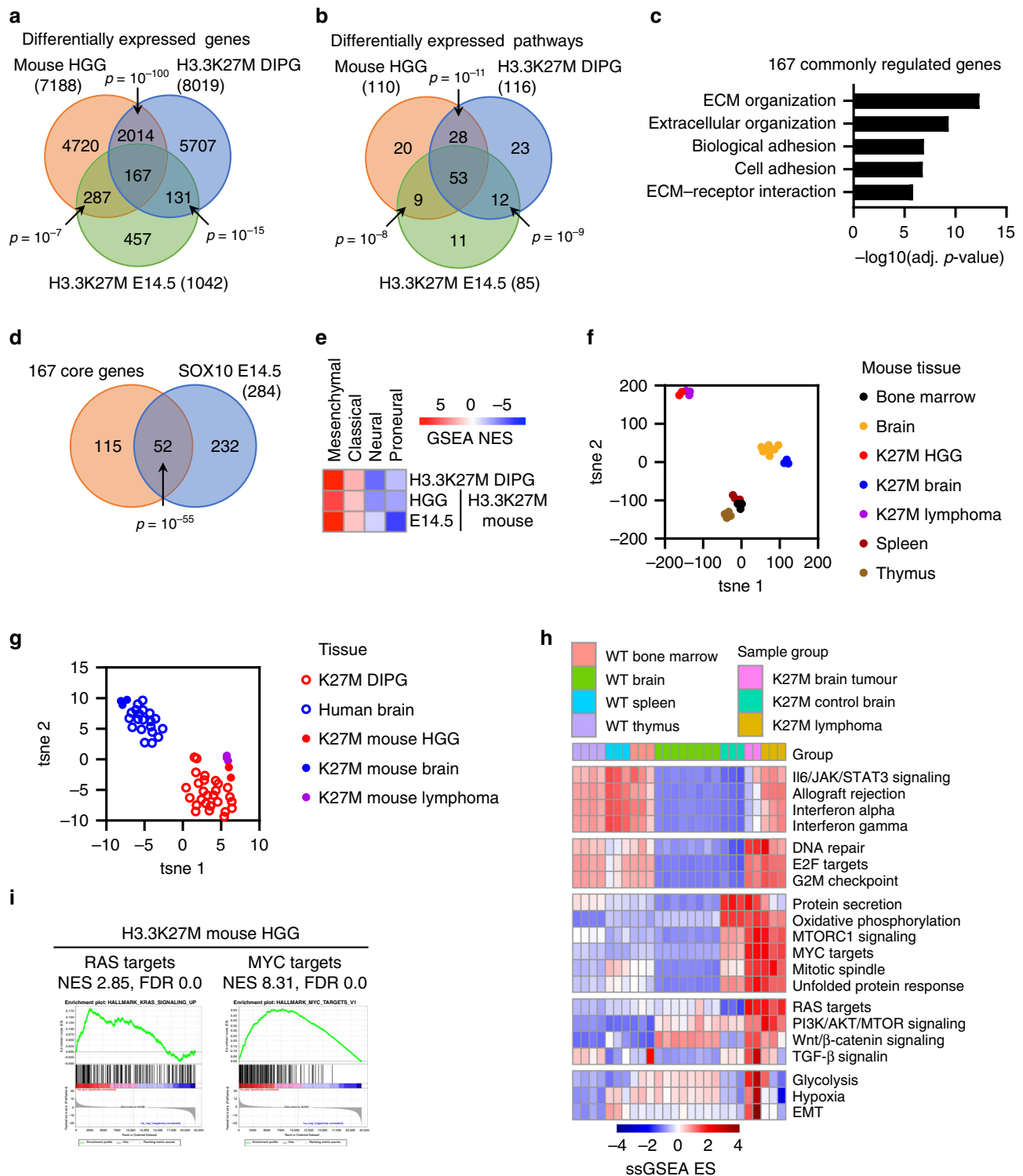


Fig. 4 H3.3K27M drives a lineage independent tumour transcriptome. a Venn diagram comparing differentially expressed genes in H3.3K27M E14.5 MB/HB and HGG with DIPG. **b** Venn diagram comparing differentially expressed Hallmark and KEGG pathways in H3.3K27M E14.5 MB/HB and HGG with DIPG. **c** Gene ontology analysis of 167 genes commonly regulated in B. **d** Venn diagram showing overlap of 167 genes commonly regulated in B with SOX10 target genes upregulated in E14.5 H3.3K27M MB/HB. **e** Heatmap showing gene set enrichment analysis (GSEA) normalised enrichment scores (NES) of glioblastoma subtype signatures. **f** t-SNE of wild type tissues (bone marrow, spleen, thymus, brain) and untransformed brain, brain tumours and lymphomas from H3.3K27M mice. **g** t-SNE of untransformed brain, brain tumours and lymphomas from H3.3K27M mice and human H3.3K27M DIPG and normal brain. **h** Heatmap of select single sample GSEA (ssGSEA) hallmark enrichment scores (ES). **i** GSEA of RAS and MYC target genes in H3.3K27M mouse HGG. FDR: false discovery rate. Source data are provided as a Source Data file. Statistical tests: Hypergeometric (**a**, **b**, **d**).

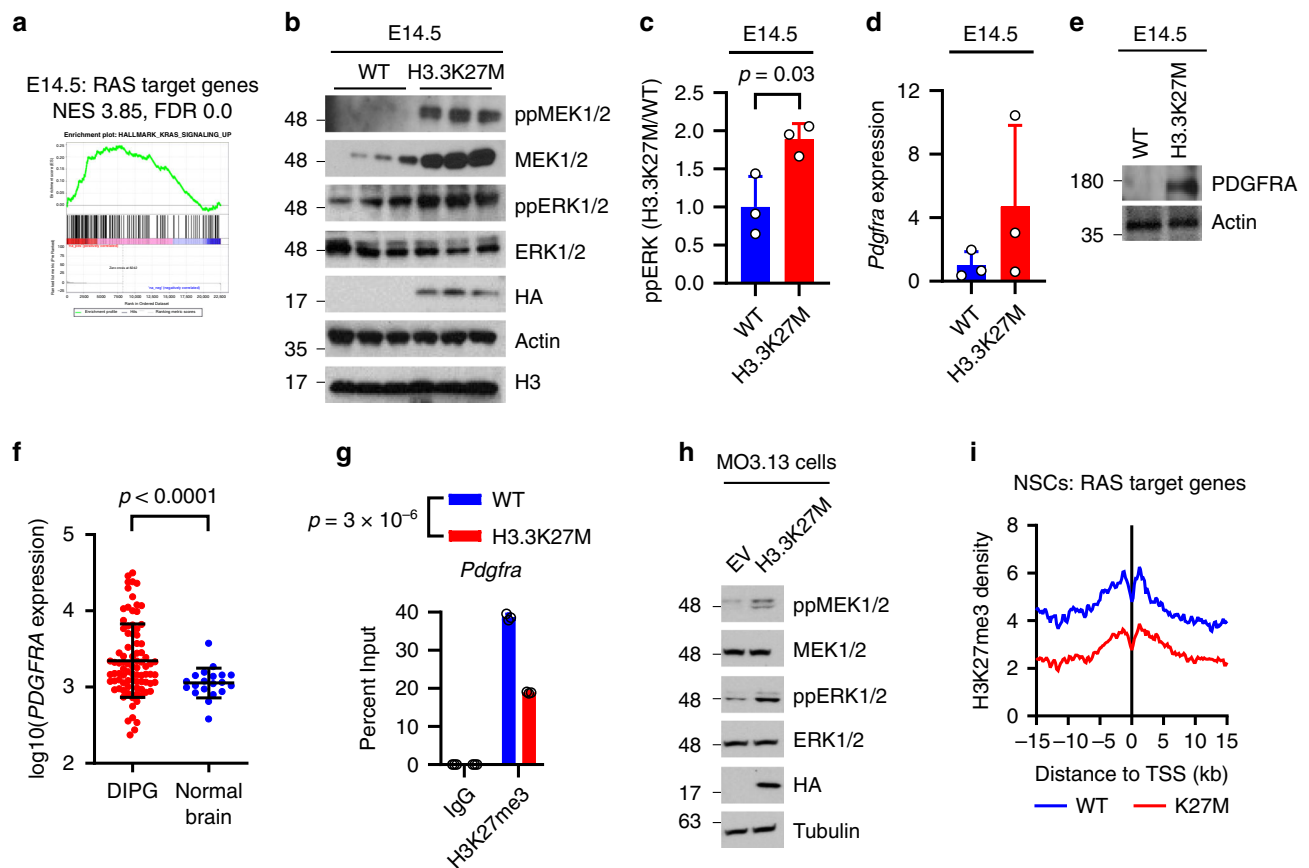


Fig. 5 Activation of RAS/MAPK is an early, epigenetically-driven effect of H3.3K27M. **a** Gene set enrichment analysis (GSEA) of RAS target genes in H3.3K27M E14.5 MB/HB. NES: Normalised Enrichment Score. FDR: false discovery rate. **b** Western blot of WT/K27M E14.5 MB/HB (results are representative of 2 independent experiments from different litters). **c** Densitometry quantifying ppERK in B as H3.3K27M vs WT (normalised to actin) and is plotted as mean \pm standard deviation ($n = 3$). **d** *Pdgfra* expression was measured by qPCR in 3 independent H3.3K27M or WT embryos, normalised to *Gapdh* and WT, and plotted as mean \pm standard deviation. **e** Western blot of H3.3K27M and WT MB/HB from littermates harvested at E14.5. Note that the actin loading control is shared with Fig. 3b (results are representative of at least 3 independent experiments). **f** *PDGFR* expression in human H3.3K27M DIPG ($n = 28$) and normal brain ($n = 20$). **g** ChIP quantifying H3K27me3 at the *Sox10* promoter in E14.5 WT or H3.3K27M MB/HB. **h** Western blot of empty vector (EV)/H3.3K27M-expressing MO3.13 cells (results are representative of 2 independent experiments). **i** H3K27me3 ChIP-Seq density was profiled ± 15 kb around the transcription start site (TSS) of *SOX10* target genes in H3.3K27M or H3.3WT NSCs⁴⁶. Source data are provided as a Source Data file. Statistical tests: t (**c**, **f**, **g**).

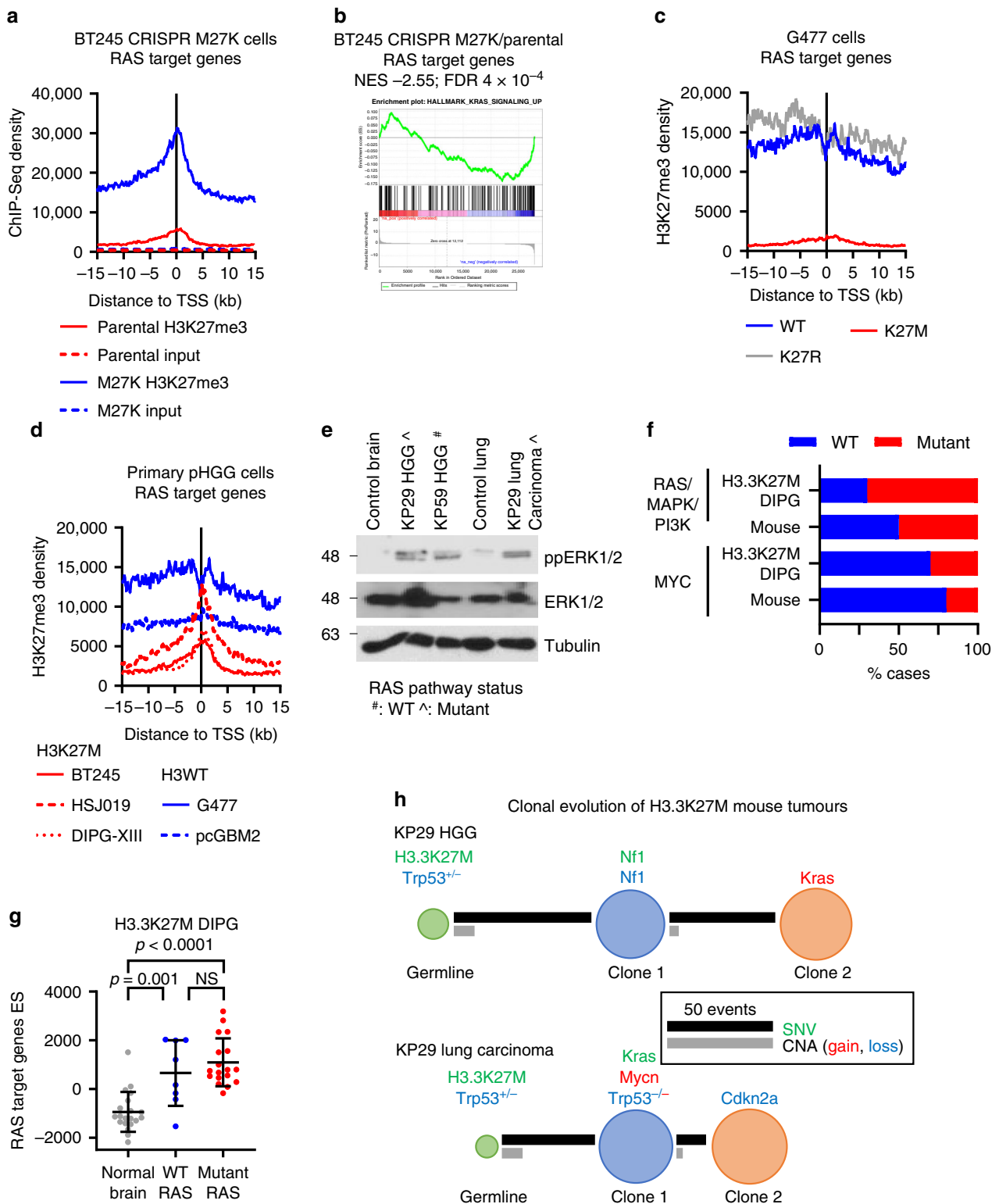
upregulated MYC targets regardless of whether they were MYC amplified (Fig. 7a and Supplementary Fig. S7a–c). Overexpression of H3.3K27M in G477 HGG cells or NSCs resulted in loss of H3K27me3 in MYC target genes compared with control cells and their upregulation in H3.3K27M-G477 cells (Fig. 7b and Supplementary Fig. S7d, e)^{46,49}. Similarly, the presence of H3.3K27M in *Trp53*^{KO}/*Pdgfra* mouse HGG led to upregulation of MYC target genes associated with loss of promoter H3K27me3 (Supplementary Fig. S7f, g)¹⁷. Conversely, depletion of *H3F3A* from H3.3K27M-mutant DIPG cells increased MYC target gene promoter H3K27me3 (Supplementary Fig. S7h)⁵⁰. Furthermore, in BT245 HGG cells, even though MYC is amplified in these cells, CRISPR-mediated removal of H3.3K27M resulted in restoration of promoter H3K27me3 and MYC target gene downregulation (Fig. 7c, d)⁴⁹. In agreement with this, primary H3.3K27M-mutant pHGG cells had reduced H3K27me3 at MYC target genes compared with H3WT cells (Fig. 7e)⁴⁹. Together, this data indicates that H3.3K27M drives epigenetic activation of the MYC pathway.

Therapeutic targeting of RAS/MYC activity in H3.3K27M-driven cancer. There is currently no clinical way to target MYC, but to test whether MYC could be a therapeutic vulnerability in

H3.3K27M-mutant cancer, we used Omomyc, a peptide-based dominant negative MYC inhibitor⁵². Omomyc expression led to downregulation of HSP90, a classical MYC target gene, in MO3.13 cells (Supplementary Fig. S7i). Importantly, H3.3K27M MO3.13 cells had significantly increased cell death in response to Omomyc expression compared with control cells (Fig. 7f).

MYC is a known effector gene of RAS signalling, which targets MYC twice (Supplementary Fig. S7j): MYC-S62 phosphorylation by ERK stabilizes MYC and prolongs its activation, and AKT suppresses GSK-3-mediated MYC-T58 phosphorylation leading to MYC degradation⁵³. To test if these mechanisms were at play in the context of H3K27M we used H3.3K27M-expressing MO3.13 cells. These had increased phospho-MYC-S62 as well as activated RAS/MAPK compared with their EV counterparts, suggesting that both H3.3K27M and RAS signalling have roles in MYC activation (Figs. 5h, 7g). In support of this, RAS and MYC activation are tightly coupled in H3.3K27M DIPG (Fig. 7h).

We then examined the effects of AKT inhibition on phospho-MYC-T58 in MO3.13 cells. As previously reported, A443654 increased phospho-AKT-S473⁵⁴. Phospho-MYC-T58 was increased in both A443654-treated WT and K27M MO3.13 cells, accompanied by a 30–40% reduction in the overall amount of MYC and HSP90 (Fig. 7i). However, H3.3K27M-MO3.13 cells



were significantly more sensitive to A443654 (IC50 29 nM vs EV IC50 72 nM, $p < 0.0001$) than WT MO3.13 cells, suggesting that K27M alone leads to increased dependency on MAPK-mediated MYC activation (Fig. 7j).

Thus, as a clinically viable alternative to directly targeting MYC, targeting either the MAPK or PI3K/AKT arms of the RAS cascade (Supplementary Fig. S7j) could be used. To test this as a potential DIPG therapy we investigated the effects of multiple MEK inhibitors and AKT inhibition on 5 H3K27M-mutant

primary DIPG cell lines. Both MEK and AKT inhibition resulted in dose-dependent DIPG cell death with IC50s in the nM range (Fig. 7k, l, Supplementary Fig. S7k, l) supporting these as important therapeutic targets for H3K27M-driven cancer.

Discussion

H3K27M mutations were first identified as high-frequency drivers of DIPG, and more recently have been found in

Fig. 6 Early epigenetic activation of RAS/MAPK pathway is later reinforced by genetic activation. **a** H3K27me3 ChIP-Seq density was profiled \pm 15 kb around the transcription start site (TSS) of RAS target genes in parental and CRISPR-M27K BT245 pHGG cells⁴⁹. **b** Gene set enrichment analysis (GSEA) of RAS target genes in CRISPR-M27K versus parental BT245 pHGG cells⁴⁹. NES: Normalised Enrichment Score. FDR: false discovery rate. **c** H3K27me3 ChIP-Seq density was profiled \pm 15 kb around the TSS of RAS target genes in parental, H3.3K27R or H3.3K27M G477 cells⁴⁹. **d** H3K27me3 ChIP-Seq density was profiled \pm 15 kb around the TSS of RAS target genes in H3K27M (red) and H3WT (blue) pHGG cells⁴⁹. **e** Western blot of control and H3.3K27M mouse tumour tissue showing increased phospho-ERK in tumours versus their respective normal counterparts (Blots were run twice with similar results). #: RAS pathway WT, ^: RAS pathway mutant. **f** Proportion of H3.3K27M DIPG or mouse tumours with RAS pathway or MYC mutations. **g** RAS target gene ssGSEA ES from RAS pathway WT ($n = 8$)/mutant ($n = 18$) H3.3K27M DIPG and normal brain ($n = 20$). ES: enrichment score. **h** Clonal evolution of single nucleotide (SNV) and copy number (CNV) variants in KP29 high-grade glioma (HGG) and lymphoma, showing known tumour drivers. The circle area of the clones and germline (normal) is proportional to the percentage of the sample comprised of each clone. Note that clone 2 evolved from clone 1, and thus contains all the alterations in clone 1. Driving events are shown. Source data are provided as a Source Data file. Statistical tests: ANOVA (**g**). NS: not significant.

additional tumour types^{2–8}. Previous pre-clinical mouse models of K27M-driven cancer focussed on generating brain tumours and revealed a cooperative effect on p53/PDGFR-driven mouse HGG^{17,19,55}. However, the oncogenic role of H3K27M itself was unclear. To investigate this we created a mouse where H3.3K27M is expressed from the *Fabp7* promoter in radial glia and astrocyte progenitors from E9.5, as well as in developing and adult non-brain tissues^{23–26,56}. H3.3K27M mice developed tumours in multiple tissues, with increased frequency and decreased latency, with and without additional *Trp53*-deficiency. Thus, this is the first demonstration that H3.3K27M is sufficient to drive tumorigenesis in the absence of other initiating mutations, establishing its role as an oncohistone. This is in keeping with recent work where removing the K27M mutation from DIPG and HGG cells by CRISPR/Cas9 inhibited their tumorigenicity⁴⁹. HGG occurred exclusively in association with *Trp53* loss in our model, while H3.3K27M alone increased lymphoma and carcinoma susceptibility. Notably, the other tumour types in which H3K27 mutations have been identified in humans are haematopoietic malignancies and carcinomas^{6–8}, perhaps explaining the spectrum of H3K27M-related cancers we saw in our model. H3K27M-mediated disruption of PRC2 in these diseases is in keeping with frequent PRC2 deregulation in haematological neoplasms and lung carcinomas, either by mutation (Supplementary Fig. S8) or differential expression^{57–61}. Finally, previous studies showed an association of high levels of H3.3 and invasive phenotypes in already developed cancers^{62,63}. While our in vitro studies support a phenotypic effect related to the mutant histone, rather than to ectopic expression of H3, our study is limited by the lack of a mouse line expressing the wild-type histone under the *Fabp7* promoter. However, transgene expression in our model was very modest compared with endogenous H3.3 and H3.3K27M in human DIPG (Supplementary Fig. S1h, i), and the phenotypes we observed were related to cancer initiation rather than to metastasis, suggesting that they are likely due to the K27M mutation rather than histone overexpression.

Although H3.3K27M expression disrupted canonical PRC2 target genes in the E14.5 MB/HB, many other genes were also upregulated, indicating that although PRC2 is important, the mutant histone must also act through additional signalling and transcriptional pathways to drive transformation. SOX10 and its target genes were epigenetically activated by H3.3K27M and, consistent with the role of SOX10 in promoting OPC commitment^{45,64,65}, we found increased expression of oligodendroglial markers at the expense of other lineages. Importantly, an OPC-like cell is hypothesised as a putative DIPG cell of origin^{34,55}, suggesting that SOX10 may have a key role in mediating the effects of H3.3K27M. This was confirmed in our cell culture model of OPC differentiation where H3K27M and SOX10

cooperated in activation of a mid-differentiation oligodendroglial transcription programme. Inhibition of SOX10 in this model also led to decreased proliferation and survival specifically in H3K27M cells, suggesting that H3K27M may use SOX10 as a proxy for maintaining oligodendroglial-like cells in a proliferative state. Given the frequent tissue specificity of transcription factors, it is likely that H3.3K27M will partner with other transcription factors in non-glial tissues.

H3.3K27M drove tumorigenesis in multiple tissues and, unexpectedly, the transcriptomes of H3.3K27M-driven tumours were far more similar to one another than to other WT tissues, including their tissues of origin. Remarkably, when comparing H3.3K27M mouse tissues with human DIPGs and normal brain, the mouse HGGs and lymphomas grouped with DIPG. Thus, oncohistone-mediated epigenetic changes override tissue-specific programmes to impose a core, lineage-independent H3.3K27M oncotranscriptome.

Among the most enriched pathways between H3.3K27M-driven mouse cancers and human DIPGs were target genes of RAS/MAPK and MYC. We found that, both in vitro and in vivo, these pathways were epigenetically activated in an H3.3K27M-dependent fashion, including through upregulation of *PDGFRA* and *MYC*. This is supported by recent work showing that H3.3K27M leads to in vitro activation of the RAS/MAPK cascade⁶⁶ and the finding that a *MYC* superenhancer was among the most highly activated by the presence of H3K27M⁶⁷. Together, this suggests that H3.3K27M-mediated epigenetic changes activate RAS/MAPK and MYC, with H3.3K27M epigenetically activating multiple members of the RAS/MAPK cascade as well as its downstream transcriptional targets. Notably, similar findings have been made in malignant peripheral nerve sheath tumours, where mutations of the SUZ12 component of the PRC2 complex result in transcriptional activation of RAS/MAPK target genes through chromatin landscape changes⁶⁸.

Interestingly, human DIPG and H3.3K27M-driven mouse tumours both develop secondary RAS/MAPK/PI3K pathway and MYC mutations. This suggests a model in which H3.3K27M initiates tumorigenesis in part through epigenetic activation of RAS and MYC and later mutational events act to lock in this activation in a portion of tumours, providing an explanation for the frequent association of *PDGFRA/PI3K* and *MYC* alterations in H3.3K27M DIPG (Supplementary Fig. S9).

Importantly, we show here for the first time that H3.3K27M alone can drive tumorigenesis. In addition to offering insight into the function of PRC2 in tumour initiation, our data suggest that H3.3K27M drives cancer by extensive transcriptome remodelling, centred on epigenetic activation of a RAS/MYC axis. Targeting these pathways was synthetically lethal with H3.3K27M providing a potential therapeutic option for treating H3K27M-driven cancers.

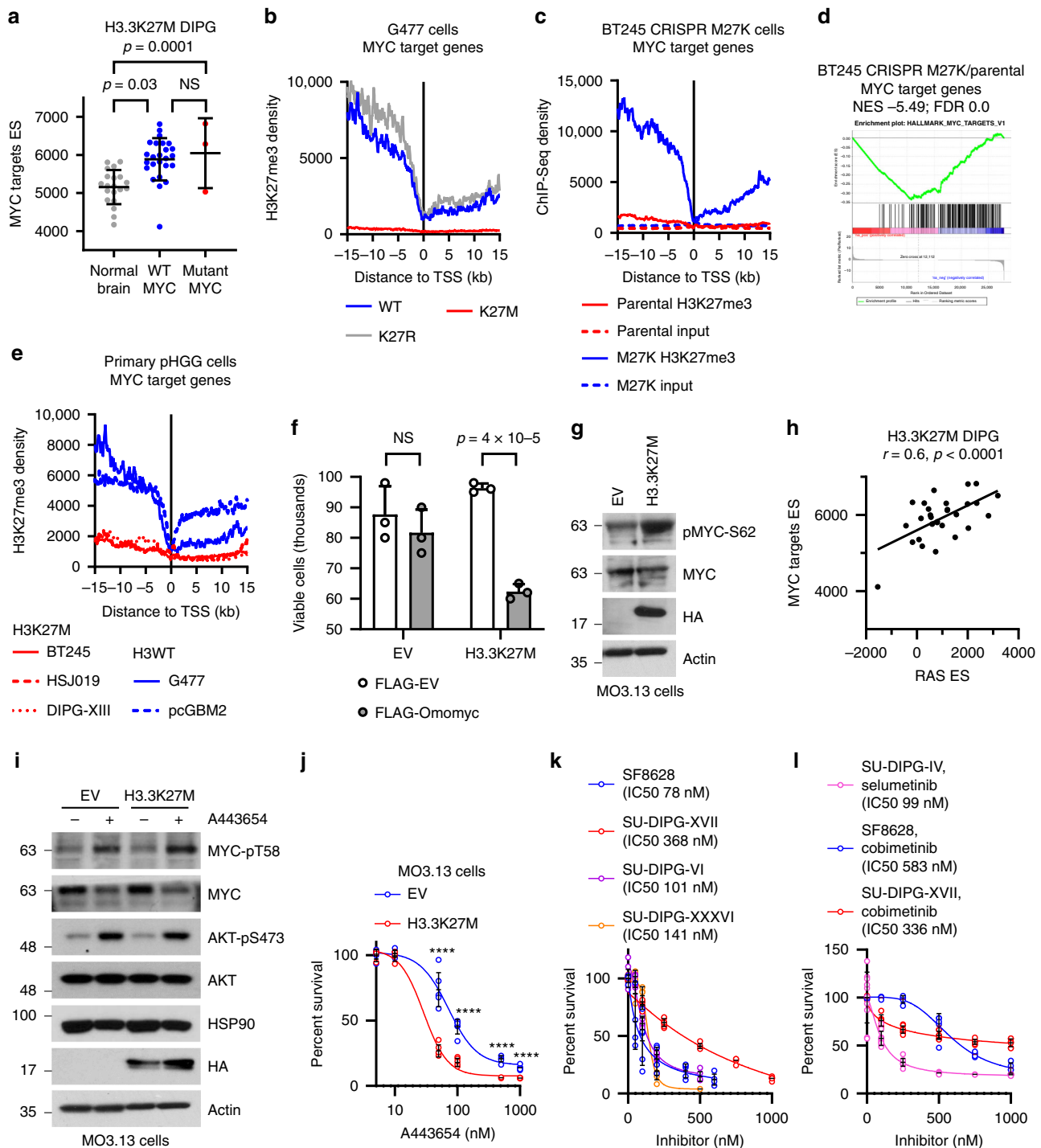


Fig. 7 Epigenetic activation of a RAS/MYC axis in H3.3K27M-driven cancers can be targeted therapeutically. **a** MYC target gene single sample gene set enrichment analysis (ssGSEA) enrichment score (ES) from MYC WT ($n = 25$)/mutant ($n = 3$) H3.3K27M DIPG and normal brain ($n = 20$). **b** H3K27me3 ChIP-Seq density was profiled ± 15 kb around the transcription start site (TSS) of MYC target genes in parental, H3.3K27R or H3.3K27M G477 cells⁴⁹. **c** H3K27me3 ChIP-Seq density was profiled ± 15 kb around the TSS of RAS target genes in parental and CRISPR-M27K BT245 pGG cells⁴⁹. **d** Gene set enrichment analysis (GSEA) of RAS target genes in CRISPR-M27K versus parental BT245 pGG cells⁴⁹. NES: Normalized Enrichment Score. FDR: false discovery rate. **e** H3K27me3 ChIP-Seq density was profiled ± 15 kb around the TSS of RAS target genes in H3K27M (red) and H3WT (blue) pGG cells⁴⁹. **f** Viability assay of empty vector (EV) or H3.3K27M MO3.13 cells 3 days post-transfection with FLAG-EV or FLAG-Omymyc plasmids. Bars show mean \pm standard deviation ($n = 3$). **g** Western blot of EV and H3.3K27M-expressing MO3.13 cells (results are representative of 2 independent experiments). **h** Scatter plot of ssGSEA ES of RAS and MYC target genes in human H3.3K27M DIPG ($n = 29$). r : Pearson correlation. **i** Western blot of EV and H3.3K27M MO3.13 cells treated or not with A443654 (50 nM) for 3 days (results are representative of 2 independent experiments). **j** Viability assay of EV and H3.3K27M MO3.13 cells treated or not with A443654 for 3 days. Bars show mean \pm standard deviation ($n = 4$). **k** Viability assays of DIPG cells treated or not with the indicated MEK inhibitor for 3 days. Bars show mean \pm standard deviation ($n \geq 5$). **l** Viability assays of DIPG cells treated or not with A443654 inhibitor for 3 days. Bars show mean \pm standard deviation ($n \geq 5$). Source data are provided as a Source Data file. Statistical tests: ANOVA (**a**, **f**), t (**h**, **j**). **** $p < 0.0001$, NS: not significant.

Methods

Ethical approval and patient samples. The Hospital for Sick Children Animal Care Committee reviewed and approved all procedures conducted on animals, which were performed in compliance with the Animals for Research Act of Ontario and the Guidelines of the Canadian Council on Animal Care. Patient material was collected from patients presenting at The Hospital for Sick Children with a diagnosis of DIPG (median age 7.1 years, 60% male, Supplementary Data 3) and after receiving informed consent. Ethics oversight was provided by the Hospital for Sick Children Research Ethics Board (#1000055059).

Transgenic construct and mice. *H3f3a* mouse cDNA with C-terminal FLAG/HA tag was cloned into pCAT3-Basic, downstream from the 1.6 kb *Fabp7* promoter, and the gel purified transgene introduced into ICR-CD1 mouse embryos by pronuclear microinjection. Of 11 positive animals, 3 male founders were chosen based on expression to develop colonies. For developmental studies littermates were used where possible, or else stage-matched CD1 control animals. B6.129S2-*Trp53*^{tm1Tyj}/J mice were a gift from Dr. Rebecca Gladly (Mt. Sinai Hospital, Toronto).

Animals were housed at The Hospital for Sick Children animal facility which operates with a 14/10 h light/dark pattern, at 45–55% humidity and within a temperature range of 22–26 °C.

Cell culture and lentivirus transduction. All cells were regularly confirmed free of mycoplasma. MO3.13 (Cedarlane) and HEK293T cells were maintained in DMEM (VWR) and 10% FBS (Wisent). DIPG cells were maintained in equal ratios of Neurobasal-A and DMEM/F12 media (Invitrogen) supplemented with 10 mM HEPES, 1 mM sodium pyruvate, 100 μM NEAA, 1 × GlutaMAX-I, 1 × antibiotic/antimycotic, 1 × vitamin A-free B-27 supplement (all from Invitrogen); 20 ng/ml EGF, 20 ng/ml FGF-basic 154, 10 ng/ml PDGF-AA, 10 ng/ml PDGF-BB (all from Shenandoah Biotech); 2 μg/ml heparin (StemCell Technologies). SU-DIPG-IV, SU-DIPG-XIII and SU-DIPG-XVII cells were a generous gift from Michele Monje (Stanford University). SF8628 DIPG cells were from Millipore. pCDH-FLAG/HA expression constructs were generated by inserting H3.3K27M cDNA between the XbaI/BamHI sites of pCDH-CMV-MCS-EF1α-copGFP (SystemBioscience) that had previously had a FLAG/HA tag inserted between the BamHI/NotI sites. Control (EV) or H3.3K27M plasmids were packaged into lentivirus by co-transfecting HEK293T cells with psPAX2 (Addgene#12260) and pMD2.G (Addgene#12259) using Lipofectamine 2000 (Invitrogen). SOX10 shRNA (TRCN0000018984 and TRCN0000018987) or control shRNA (shRNA) plasmids were purchased from Sigma and packed as described. Lentiviral particles were precipitated with Lenti-X Concentrator (Clontech) and resuspended in OptiMem (Invitrogen). For differentiation protocol MO3.13 cells were seeded at 40% confluence and cultured in regular (DMEM supplemented with 10% FBS) or OL differentiation media (DMEM supplemented with 100 nm phorbol 12-myristate 13-acetate [PMA; Sigma]) for 4 and 10 days respectively with daily media change.

Experiments were carried out 4–5 passages post-transduction. Inhibitors were from: Cayman Chemical Company (A443654, cobimetinib), AdipoGen Life Sciences (selumetinib), Sigma (trametinib). Growth curves were generated using trypan blue exclusion assay and Vi-CellXR (Beckman Coulter).

Western blot analysis. Whole cell lysates of organs and cells were prepared in 2x SDS lysis buffer (20 mM Tris [pH 7.4], 20 mM EDTA, 2% SDS, 20% glycerol) and concentration determined by DC Protein Assay (Bio-Rad). 30 μg of protein was resolved on 10–20% SDS-PAGE and transferred to PVDF membranes that were blocked and incubated with antibodies diluted in 3% BSA in TBS-T. Binding was detected with enhanced chemiluminescence (Pierce).

Immunohistochemistry. Organs and tissues were fixed in 4% PFA and embedded in paraffin. Antigen retrieval using heat and citrate buffer was included for all antibodies. Signal was detected with DAB peroxidase substrate (Vector Laboratories). Images were captured on a Nikon Eclipse E600 microscope.

RNA sequencing. Total RNA was prepared with RNeasy kit (Qiagen) and quality confirmed with Bioanalyzer 2100 (Agilent). TruSeq Stranded Total RNA Library Prep with Ribo-Zero Gold (Illumina, CA, USA) were constructed and sequenced on Illumina HiSeq 2500 at the Hospital for Sick Children (Toronto; paired end 100 bp [E14.5 and human] or 125 bp [human] reads) or Illumina NextSeq 500 at the Princess Margaret Genomics Centre (Toronto; paired end 75 bp reads [mouse tumours]).

Reads were trimmed with Trimmomatic-v0.32⁶⁹ and aligned to GRCm38-v68 (mouse) or GRCh37-v75 (human) using STAR v2.5.0⁷⁰ in two-pass mode; duplicate reads were marked with Picard-v2.5.0. Gene expression was counted with HTSeq⁷¹, and differential expression calculated with edgeR⁷². Genes with absolute fold-change > 1 and Benjamini-Hochberg adjusted p-value < 0.05 were classed differentially expressed. Pathways were analysed with DAVID⁷³. Genes were ranked by multiplying their fold-change sign with the -log₁₀(adjusted p-value) for pre-ranked GSEA³⁷, using human homologues of mouse genes obtained from Ensembl. For ssGSEA, reads were aligned to the transcriptome using RSEM-v1.2⁷⁴. Genes with mean FPKM < 1 were discarded, and genes with duplicated names were filtered to keep the most expressed gene. SOX10 target genes were from the

Harmonizome⁷⁵. *Fabp7* RNA-Seq expression data was from the Gene Expression Database⁷⁶.

Network analysis. Transcription factor (TF) networks were scored on three metrics, similar to previous methods⁷⁷, with improvements to network weighting by gene differential expression. Differential gene expression scores were calculated as for pre-ranked GSEA. Networks of TF-DNA and TF-Protein interaction edges were constructed from MARA⁷⁸ and String-DB⁷⁹, respectively, allowing a maximal edge distance of 3 from the root TF. The network score ($N_{t,n}$) was computed by

$$N_{t,n} = \sum_{r \in V_t} \frac{S_r \cdot S_n}{D_{r,n} \cdot L_{r,n}}$$

where $r \in V_t$ is the set of all genes (r) in the local subnetwork of transcription factor t ; S_r is the differential expression gene score, S_n is the MARA/String relationship score; $D_{r,n}$ and $L_{r,n}$ is the edge distance of gene r from t and the out-degree of the parent node in the network, respectively. Each TF network was scored as the aggregate rank of each sub-score in decreasing order, such that the higher the rank, the stronger the effect of the TF influence among differentially expressed genes.

End-point PCR and Q-PCR. Total RNA was reverse transcribed using Reverse Transcription kit (Applied Biosystems). End point PCR was performed for 28 cycles unless indicated otherwise. End-point PCR-validated primers were used for qPCR with iTaq Universal SYBR green supermix (Bio-Rad).

Mouse exome sequencing. DNA was extracted from frozen tissue samples with DNeasy kit (Qiagen). Exome libraries were generated with the SureSelect Mouse All Exon Kit (Agilent). Paired end 125 bp Illumina HiSeq 2500 sequencing was done at The Hospital for Sick Children. We sequenced a pool of normal CD1 mice because there is no available CD1 reference genome or genome-wide SNP analysis.

Reads were trimmed (Trimmomatic-v0.32⁶⁹) and aligned GRCm38 with bwa-v0.7.8⁸⁰. Indel realignment and base quality recalibration was performed with GATK-v3.6.0⁸¹ and duplicate reads marked. Sequencing depth was 87–115 × (normal) and 86–134 × (tumour).

Somatic variants were called with VarScan-v2.3.8⁸² and Mutect2⁸³, retaining those identified by both. For unmatched tumours, variants were called individually against all normals including the CD1 pool, retaining those identified with both tools against every normal and additionally discarding known variants in other mouse strains, as we could not exclude the possibility that these are also present in a particular CD1 mouse. Variants with >10x coverage in both tumour and normal samples, a minimum tumour variant allele frequency (VAF) of 0.05 and maximum normal VAF of 0.01 were annotated using SnpEFF-v4.3k⁸⁴. Variants were compared with known human cancer variants using the COSMIC-v81⁸⁵. Clonal evolution of tumours with a matched normal was analysed with SuperFreq⁸⁶. Copy number variants were identified using both on- and off-target reads with CNVkit v0.8.6⁸⁷.

Human exome sequencing. DNA was extracted from frozen tissue samples with DNeasy kit (Qiagen). Libraries were created with Ion TargetSeq Exome 50 Mb library (ThermoFisher), sequenced on Ion Proton machines (ThermoFisher), and aligned to human genome build hg19 with Torrent Suite Software (ThermoFisher) at The Hospital for Sick Children. Variants were called with VarScan and annotated with SnpEFF. RAS pathway and MYC mutant samples were determined by the presence of an alteration in a core RAS/MAPK/PI3K pathway gene (Supplementary Data 4) or MYC, respectively. These were restricted to SNVs/indels that introduced missense, frameshift, nonsense or splice site mutations at variant-allele frequency >0.2 and with coverage >20, a copy number gain with 5+ copies, or a homozygous deletion, had to be present in the sample for any pathway gene. Wild-type samples had all pathway genes free of SNV/indels and copy number changes.

Statistical analysis. Unless otherwise stated, all p -values were calculated by two-tailed t -tests, not assuming equal variance between samples.

Reporting summary. Further information on research design is available in the Nature Research Reporting Summary linked to this article.

Data availability

Raw mouse WES and RNA-seq data is available from the Gene Expression Omnibus (GEO), accession GSE120884. Human WES and RNA-seq data is available from the European Genomics Archive, accession EGAD00001006450 (<https://ega-archive.org>). Publicly available data was from GEO (<https://www.ncbi.nlm.nih.gov/geo> accessions GSE115875, GSE85390, GSE108364) or <https://datahub-jv64f4mbl.udes.genap.ca>, and is referenced both within the article and in Supplementary Table S8. All other information supporting the findings of this study are available within the article, its Supplementary Information files, a Source Data file and from the corresponding author upon reasonable request. Source data are provided with this paper.

Code availability

The custom python code for performing TF network analysis is available from https://github.com/chawkins-lab/tf_circuit_driver.

Received: 10 February 2020; Accepted: 10 November 2020;

Published online: 04 December 2020

References

- Rubin, G. et al. Pediatric brain stem gliomas: an update. *Child's Nerv. Syst.* **14**, 167–173 (1998).
- Khuong-Quang, D. A. et al. K27M mutation in histone H3.3 defines clinically and biologically distinct subgroups of pediatric diffuse intrinsic pontine gliomas. *Acta Neuropathol.* **124**, 439–447 (2012).
- Schwartzentruber, J. et al. Driver mutations in histone H3.3 and chromatin remodelling genes in paediatric glioblastoma. *Nature* **482**, 226–231 (2012).
- Lehnertz, B. et al. H3K27M/I mutations promote context-dependent transformation in acute myeloid leukemia with RUNX1 alterations. *Blood* **130**, 2204–2214 (2017).
- Nacev, B. A. et al. The expanding landscape of ‘oncohistone’ mutations in human cancers. *Nature* **567**, 473–478 (2019).
- Boileau, M. et al. Mutant H3 histones drive human pre-leukemic hematopoietic stem cell expansion and promote leukemic aggressiveness. *Nat. Commun.* **10**, 2891 (2019).
- Kalender Atak, Z. et al. Comprehensive analysis of transcriptome variation uncovers known and novel driver events in T-cell acute lymphoblastic leukemia. *PLoS Genet.* **9**, e1003997 (2013).
- Yu, S. et al. Low frequency of H3.3 mutations and upregulated DAXX expression in MDS. *Blood* **121**, 4009–4012 (2019).
- Soshnev, A. A., Josefowicz, S. Z. & Allis, C. D. Greater than the sum of parts: complexity of the dynamic epigenome. *Mol. Cell* **62**, 681–694 (2016).
- Margueron, R. & Reinberg, D. The polycomb complex PRC2 and its mark in life. *Nature* **469**, 343–349 (2011).
- Zhang, Y. & Reinberg, D. Transcription regulation by histone methylation: Interplay between different covalent modifications of the core histone tails. *Genes Dev.* **15**, 2343–2360 (2001).
- Lewis, P. W. et al. Inhibition of PRC2 activity by a gain-of-function H3 mutation found in pediatric glioblastoma. *Science* **340**, 857–861 (2013).
- Bender, S. et al. Reduced H3K27me3 and DNA hypomethylation are major drivers of gene expression in K27M mutant pediatric high-grade gliomas. *Cancer Cell* **24**, 660–672 (2013).
- Piunti, A. et al. Therapeutic targeting of polycomb and BET bromodomain proteins in diffuse intrinsic pontine gliomas. *Nat. Med.* **23**, 493–500 (2017).
- Nikbakht, H. et al. Spatial and temporal homogeneity of driver mutations in diffuse intrinsic pontine glioma. *Nat. Commun.* **7**, 11185 (2016).
- Hoffman, L. M. et al. Spatial genomic heterogeneity in diffuse intrinsic pontine and midline high-grade glioma: implications for diagnostic biopsy and targeted therapeutics. *Acta Neuropathol. Commun.* **4**, 1 (2016).
- Larson, J. D. et al. Histone H3.3 K27M accelerates spontaneous brainstem glioma and drives restricted changes in bivalent gene expression. *Cancer Cell* **35**, 140–155 (2019).
- Cordero, F. J. et al. Histone H3.3K27M represses p16 to accelerate gliomagenesis in a murine model of DIPG. *Mol. Cancer Res.* **15**, 1243–1254 (2018).
- Pathania, M. et al. H3.3 K27M Cooperates with Trp53 loss and PDGFRA gain in mouse embryonic neural progenitor cells to induce invasive high-grade gliomas. *Cancer Cell* **32**, 684–700 (2017).
- Patel S. K. et al. Generation of diffuse intrinsic pontine glioma mouse models by brainstem targeted in utero electroporation. *Neuro. Oncol.* **22**, 381–392 (2019).
- Buczkwicz, P. et al. Genomic analysis of diffuse intrinsic pontine gliomas identifies three molecular subgroups and recurrent activating ACVR1 mutations. *Nat. Genet.* **46**, 451–456 (2014).
- Mackay, A. et al. Integrated molecular meta-analysis of 1,000 pediatric high-grade and diffuse intrinsic pontine glioma. *Cancer Cell* **32**, 520–537 (2017).
- Tokuda, N. et al. Identification of FABP7 in fibroblastic reticular cells of mouse lymph nodes. *Histochem. Cell Biol.* **134**, 445–452 (2010).
- Wagner, A. J. et al. Genetic analysis of congenital cystic adenomatoid malformation reveals a novel pulmonary gene: fatty acid binding protein 7 (brain type). *Pediatr. Res.* **64**, 11–16 (2008).
- Su, X. et al. Characterization of fatty acid binding protein 7 (FABP7) in the murine retina. *Investig. Ophthalmol. Vis. Sci.* **57**, 3397–3408 (2016).
- Miyazaki, H. et al. Fatty acid binding protein 7 regulates phagocytosis and cytokine production in kupffer cells during liver injury. *Am. J. Pathol.* **184**, 2505–2515 (2014).
- Giknis, M. L. A. & Clifford, C. B. Spontaneous Neoplastic Lesions in the CrI: CD-1(ICR) Mouse in Control Groups from 18 Month to 2 year Studies. *Charles Rivers Lab.* <https://www.crivier.com/sites/default/files/resources/SpontaneousNeoplasticLesionsintheCrICD-1ICRMouseinControlGroupsfrom18Monthto2YearStudies%E2%80%9494March2005.pdf> (2005).
- Forster, R., Thirion-Delalande, C., Palate, B. & Le Bigot, J. F. Lifetime carcinogenicity studies in the CD-1 mouse: Historical data for survival and neoplasms. *CitoxLab* **229**, S148 (2014).
- Son, W. C. & Gopinath, C. Early occurrence of spontaneous tumors in CD-1 mice and Sprague-Dawley rats. *Toxicol. Pathol.* **32**, 371–374 (2004).
- Kohnken, R., Porcu, P. & Mishra, A. Overview of the use of murine models in leukemia and lymphoma research. *Front. Oncol.* **7**, 22 (2017).
- Jacks, T. et al. Tumor spectrum analysis in p53-mutant mice. *Curr. Biol.* **4**, 1–7 (1994).
- Lang, G. A. et al. Gain of function of a p53 hot spot mutation in a mouse model of Li-Fraumeni syndrome. *Cell* **119**, 861–872 (2004).
- Venot, C. et al. The requirement for the p53 proline-rich functional domain for mediation of apoptosis is correlated with specific PIG3 gene transactivation and with transcriptional repression. *EMBO J.* **17**, 4668–4679 (1998).
- Nagaraja, S. et al. Histone Variant and Cell Context Determine H3K27M Reprogramming of the Enhancer Landscape and Oncogenic State Resource Histone Variant and Cell Context Determine H3K27M Reprogramming of the Enhancer Landscape and Oncogenic State. *Mol. Cell* **76**, 965–980 (2019).
- Li, J. Y., Patterson, M., Mikkola, H. K. A., Lowry, W. E. & Kurdistani, S. K. Dynamic distribution of linker histone H1.5 in cellular differentiation. *PLoS Genet.* **8**, e1002879 (2012).
- Prince, V. E. Hox genes and segmental patterning of the vertebrate hindbrain. *Am. Zool.* **38**, 634–646 (1998).
- Subramanian, A. et al. Gene set enrichment analysis: a knowledge-based approach for interpreting genome-wide expression profiles. *Proc. Natl Acad. Sci. USA* **102**, 15545–15550 (2005).
- Liberzon, A. et al. The Molecular Signatures Database (MSigDB) hallmark gene set collection. *Cell Syst.* **1**, 417–425 (2015).
- Cahoy, J. D. et al. A transcriptome database for astrocytes, neurons, and oligodendrocytes: a new resource for understanding brain development and function. *J. Neurosci.* **28**, 264–278 (2008).
- Accetta, R. et al. Oxygen species derived from NOX3 and NOX5 drive differentiation of human oligodendrocytes. *Front. Cell. Neurosci.* **10**, 146 (2016).
- Santos, G., Barateiro, A., Gomes, C. M., Brites, D. & Fernandes, A. Impaired oligodendrogenesis and myelination by elevated S100B levels during neurodevelopment. *Neuropharmacology* **129**, 69–83 (2018).
- Srinivasan, R. et al. Genome-wide analysis of EGR2/SOX10 binding in myelinating peripheral nerve. *Nucleic Acids Res.* **40**, 6449–6460 (2012).
- García-León, J. A. et al. SOX10 single transcription factor-based fast and efficient generation of oligodendrocytes from human pluripotent stem cells. *Stem Cell Rep.* **10**, 655–672 (2018).
- Schaefer, T. & Lengerke, C. SOX2 protein biochemistry in stemness, reprogramming, and cancer: the PI3K/AKT/SOX2 axis and beyond. *Oncogene* **39**, 278–292 (2020).
- Pozniak, C. D. et al. Sox10 directs neural stem cells toward the oligodendrocyte lineage by decreasing Suppressor of Fused expression. *Proc. Natl Acad. Sci. USA* **107**, 21795–21800 (2010).
- Mohammad, F. et al. EZH2 is a potential therapeutic target for H3K27M-mutant pediatric gliomas. *Nat. Med.* **23**, 483–492 (2017).
- Verhaak, R. G. W. et al. Integrated genomic analysis identifies clinically relevant subtypes of glioblastoma characterized by abnormalities in PDGFRA, IDH1, EGFR, and NF1. *Cancer Cell* **17**, 98–110 (2010).
- Li, B. et al. A comprehensive mouse transcriptomic BodyMap across 17 tissues by RNA-seq. *Sci. Rep.* **7**, 4200 (2017).
- Harutyunyan, A. S. et al. H3K27M induces defective chromatin spread of PRC2-mediated repressive H3K27me2/me3 and is essential for glioma tumorigenesis. *Nat. Commun.* **10**, 1262 (2019).
- Silveira, A. B. et al. H3.3 K27M depletion increases differentiation and extends latency of diffuse intrinsic pontine glioma growth in vivo. *Acta Neuropathol.* **137**, 637–655 (2020).
- Zarghooni, M. et al. Whole-genome profiling of pediatric diffuse intrinsic pontine gliomas highlights platelet-derived growth factor receptor α and poly (ADP-ribose) polymerase as potential therapeutic targets. *J. Clin. Oncol.* **28**, 1337–1344 (2010).
- Soucek, L. et al. Design and properties of a Myc derivative that efficiently homodimerizes. *Oncogene* **17**, 2463–2472 (1998).
- Sears, R. et al. Multiple Ras-dependent phosphorylation pathways regulate Myc protein stability. *Genes Dev.* **14**, 2501–2514 (2000).

54. Han, E. et al. Akt inhibitor A-443654 induces rapid Akt Ser-473 phosphorylation independent of mTORC1 inhibition. *Oncogene* **26**, 5655–5661 (2007).
55. Monje, M. et al. Hedgehog-responsive candidate cell of origin for diffuse intrinsic pontine glioma. *Proc. Natl Acad. Sci. USA* **108**, 4453–4458 (2011).
56. Muñoz, D. M. et al. Differential transformation capacity of neuro-glial progenitors during development. *Proc. Natl Acad. Sci. USA* **110**, 14378–14383 (2013).
57. Bödör, C. et al. EZH2 mutations are frequent and represent an early event in follicular lymphoma EZH2 mutations are frequent and represent an early event in follicular lymphoma. *Lymphoid Neoplasia* **122**, 3165–3168 (2014).
58. Melnick, R. S. & Epigenetics A and B-cell lymphoma. *Curr. Opin. Hematol.* **18**, 293–299 (2011).
59. Hu, D. & Shilatifard, A. Epigenetics of hematopoiesis and hematological malignancies. *Genes Dev.* **30**, 2021–2041 (2016).
60. Stransky, N. et al. The mutational landscape of head and neck squamous cell carcinoma. *Science* **333**, 1157–1160 (2012).
61. Sato, T. et al. PRC2 overexpression and PRC2-target gene repression relating to poorer prognosis in small cell lung cancer. *Sci. Rep.* **3**, 1–9 (2013).
62. Gomes, A. P. et al. Dynamic incorporation of histone H3 variants into chromatin is essential for acquisition of aggressive traits and metastatic colonization. *Cancer Cell* **36**, 402–417.e13 (2019).
63. Park, S. M. et al. Histone variant H3F3A promotes lung cancer cell migration through intronic regulation. *Nat. Commun.* **7**, 1–14 (2016).
64. Hornig, J. et al. The transcription factors Sox10 and Myrf define an essential regulatory network module in differentiating oligodendrocytes. *PLoS Genet.* **9**, e1003907 (2013).
65. Finzsch, M., Stolt, C. C., Lommes, P. & Wegner, M. Sox9 and Sox10 influence survival and migration of oligodendrocyte precursors in the spinal cord by regulating PDGF receptor expression. *Development* **135**, 637–646 (2008).
66. Koncar, R. F. et al. Identification of novel RAS signaling therapeutic vulnerabilities in diffuse intrinsic pontine gliomas. *Cancer Res.* **79**, 4026–4041 (2019).
67. Gliomas, H. K. M. et al. Pervasive H3K27 acetylation leads to ERV expression and a therapeutic vulnerability in article pervasive H3K27 acetylation leads to ERV expression and a therapeutic vulnerability in H3K27M gliomas. *Cancer Cell* **35**, 782–797 (2019).
68. De Raedt, T. et al. PRC2 loss amplifies Ras-driven transcription and confers sensitivity to BRD4-based therapies. *Nature* **514**, 247–251 (2014).
69. Bolger, A. M., Lohse, M. & Usadel, B. Trimmomatic: a flexible trimmer for Illumina sequence data. *Bioinformatics* **30**, 2114–2120 (2014).
70. Dobin, A. et al. STAR: Ultrafast universal RNA-seq aligner. *Bioinformatics* **29**, 15–21 (2013).
71. Anders, S., Pyl, P. T. & Huber, W. HTSeq-A Python framework to work with high-throughput sequencing data. *Bioinformatics* **31**, 166–169 (2015).
72. Robinson, M. D., McCarthy, D. J. & Smyth, G. K. edgeR: a Bioconductor package for differential expression analysis of digital gene expression data. *Bioinformatics* **26**, 139–140 (2009).
73. Huang, D. W., Sherman, B. T. & Lempicki, R. Systematic and integrative analysis of large gene lists using DAVID bioinformatic resources. *Nat. Protoc.* **4**, 44–57 (2009).
74. Li, B. & Dewey, C. N. RSEM: Accurate transcript quantification from RNA-Seq data with or without a reference genome. *BMC Bioinformatics* **12**, 323 (2011).
75. Rouillard, A. D. et al. The harmonizome: a collection of processed datasets gathered to serve and mine knowledge about genes and proteins. *Database* **2016**, 1–16 (2016).
76. Smith, C. M. et al. The mouse Gene Expression Database (GXD): 2019 update. *Nucleic Acids Res.* **47**, D774–D779 (2019).
77. Rackham, O. J. L. et al. A predictive computational framework for direct reprogramming between human cell types. *Nat. Genet.* **48**, 331–335 (2016).
78. Balwiercz, P. J. et al. ISMARA: automated modeling of genomic signals as a democracy of regulatory motifs. *Genome Res.* **24**, 869–884 (2014).
79. Szklarczyk, D. et al. STRING v11: Protein-protein association networks with increased coverage, supporting functional discovery in genome-wide experimental datasets. *Nucleic Acids Res.* **47**, D607–D613 (2019).
80. Li, H. & Durbin, R. Fast and accurate short read alignment with Burrows-Wheeler transform. *Bioinformatics* **25**, 1754–1760 (2009).
81. Schmidt, S. The Genome Analysis Toolkit: A MapReduce framework for analyzing next-generation DNA sequencing data. *Proc. Int. Conf. Intellect. Cap., Knowl. Manag. Organ. Learn.* **20**, 254–260 (2009).
82. Koboldt, D. C. et al. VarScan 2: Somatic mutation and copy number alteration discovery in cancer by exome sequencing VarScan 2: Somatic mutation and copy number alteration discovery in cancer by exome sequencing. *Genome Res.* **22**, 568–576 (2012).
83. Cibulskis, K. et al. Sensitive detection of somatic point mutations in impure and heterogeneous cancer samples. *Nat. Biotechnol.* **31**, 213–219 (2013).
84. Mellin, J. R. & Cossart, P. A program for annotating and predicting the effects of single nucleotide polymorphisms, SnpEff: SNPs in the genome of *Drosophila melanogaster* strain w1118; iso-2; iso-3. *Fly.* **6**, 80–92 (2012).
85. Forbes, S. A. et al. COSMIC: Somatic cancer genetics at high-resolution. *Nucleic Acids Res.* **45**, D777–D783 (2017).
86. Flensburg, C., Sargeant, T., Oshlack, A. & Majewski, I. SuperFreq: Integrated mutation detection and clonal tracking in cancer. *PLoS Comput. Biol.* **16**, e1007603 (2020).
87. Talevich, E., Shain, A. H., Botton, T. & Bastian, B. C. CNVkit: genome-wide copy number detection and visualization from targeted DNA sequencing. *PLoS Comput. Biol.* **12**, e1004873 (2016).

Acknowledgements

We would like to thank Hawkins lab members past and present for insightful comments and discussions. We would also like to thank Dr. Rebecca Gladly for providing the B6.129S2-*Trp53^{tm1Tyj}/J* mice. This work was funded by Canadian Cancer Society grant numbers 702296 and 706160, ChadTough foundation, Meagan's Walk and Nelina's Hope Pediatric Brain Tumor Foundation. Funding: Canadian Cancer Society Research Institute (702296 and 706160), ChadTough foundation, Meagan's Walk and Nelina's Hope Pediatric Brain Tumour Foundation.

Author contributions

Conceptualisation: S.P., R.S., C.H., Methodology: S.P., R.S., T.B., P.R., S.A., C.H., Formal analysis: R.S., C.L., P.P., Investigation: S.P., R.S., T.B., J.S., P.R., B.K., S.R., L.P., M.Y., S.M., D.S., Visualisation: S.P., R.S., P.R., B.K., C.L., P.P., Writing: Original Draft, S.P., R.S., C.H., Writing: Review and Editing, S.P., R.S., P.R., A.H., C.H., Supervision: C.H., Funding Acquisition: C.H.

Competing interests

The authors declare no competing interests.

Additional information

Supplementary information is available for this paper at <https://doi.org/10.1038/s41467-020-19972-7>.

Correspondence and requests for materials should be addressed to C.H.

Peer review information *Nature Communications* thanks Oren Becher and the other anonymous reviewer(s) for their contribution to the peer review of this work.

Reprints and permission information is available at <http://www.nature.com/reprints>

Publisher's note Springer Nature remains neutral with regard to jurisdictional claims in published maps and institutional affiliations.



Open Access This article is licensed under a Creative Commons Attribution 4.0 International License, which permits use, sharing, adaptation, distribution and reproduction in any medium or format, as long as you give appropriate credit to the original author(s) and the source, provide a link to the Creative Commons license, and indicate if changes were made. The images or other third party material in this article are included in the article's Creative Commons license, unless indicated otherwise in a credit line to the material. If material is not included in the article's Creative Commons license and your intended use is not permitted by statutory regulation or exceeds the permitted use, you will need to obtain permission directly from the copyright holder. To view a copy of this license, visit <http://creativecommons.org/licenses/by/4.0/>.

© The Author(s) 2020